Three-dimensional acoustic metamaterials with topological states of different orders and multidirectional waveguiding

Guifeng Wang [1], Zhenyu Chen [2,*], Zhifei Shi [3], and C. W. Lim [1,†]

[1] *Department of Architecture and Civil Engineering, City University of Hong Kong, Tat Chee Avenue, Kowloon, Hong Kong SAR, People's Republic of China*

[2] *School of Civil Engineering, Southeast University, Nanjing 210096, People's Republic of China*

[3] *Institute of Smart Materials and Structures, Beijing Jiaotong University, Beijing 100044, People's Republic of China*

(Received 13 December 2023; revised 3 March 2024; accepted 3 April 2024; published 24 April 2024)

The attainment of high-quality wave concentration and manipulation has always been considered as state-of-the-art technology, especially for integrated photonics and phononics. However, the prevention of energy loss caused by backscattering or imperfections remains a grand challenge. With the development of the topological phase of matter, the emergence of topological insulators that support robust conductive edge states but insulating bulk waves provides a possible solution. Nevertheless, the existing topological insulators can only achieve wave manipulation in two-dimensional (2D) models along specific hinges. To achieve lossless waveguiding in three-dimensional space, an acoustic topological insulator with three degrees of freedom is established. The theoretical dispersion relation is analyzed by introducing an equivalent electric circuit system. The topological states, including point corner states, one-dimensional hinge states, and 2D surface states are realized by tweaking the intra- and intercell couplings. Abundant wave propagation behaviors such as surface-restricted, edge-restricted, and corner-restricted wave transportation are respectively achieved in the first-, second-, and third-order topological insulators. The twisted 3D path waveguiding without significant energy leaking into surface and bulk is finally demonstrated. This sound transportation phenomenon may provide a paradigm and design idea for integrated acoustic devices with unconventional functions.

DOI: 10.1103/PhysRevB.109.144307

I. INTRODUCTION

The topological phases of matter, initially proposed in electronic systems, have significantly depended on the comprehension of condensed matter physics, and gave birth to topological insulators (TIs) [1–4]. Ascribing to the unprecedented boundary states, TIs, which are conductive in edges but insulating for bulk, have also attracted tremendous research interest in classical wave applications such as optical systems [5,6], elastic systems [7–9], and acoustic systems [10,11]. One hallmark of TIs is the topologically protected interface modes (TPIMs) localized at the interface of two TIs with distinct topological phases, leading to robust waveguiding that is immune to defects, disorders, and backscattering [12–14]. For example, Huo *et al.* [15] demonstrated three-dimensional (3D) robust layer-selective elastic wave propagation by designing a bilayer-stacked platelike structure. Due to their peculiar properties, TIs are highly desired in numerous application systems that are related to wave manipulation such as structural health monitoring [16], noise/vibration control [17,18], and energy harvesting [19,20]. The key point for designing a TI is breaking structure symmetry, including inversion symmetry, time-reversal symmetry, or crystalline symmetry. However, all the aforementioned approaches follow bulk-boundary correspondence, thus requiring gapless topological states [21], which is one dimension lower than the dimension of the TI. For instance, a 3D TI only presents two-dimensional (2D) gapless topological surface states, while a 2D TI only presents one-dimensional (1D) gapless topological surface states.

Recently, a new paradigm of TI, namely, higher-order topological insulators (HOTIs), which feature unconventional bulk-boundary correspondence, has been introduced [22,23]. In principle, a nth-order dD HOTI can exhibit (d-1)D, (d-2)D, …, (d-n + 1)D gapped topological states and (d-n)D gapless topological states, which are the so-called dimensional hierarchy of HOTI [24,25]. For example, 1D topological hinge states, and zero-dimensional (0D) topological corner states can coexist in principle in a second-order 2D TI. The emergence of HOTIs indisputably broadens the spectrum of topological materials and offers a methodology to manipulate waves on surfaces, hinges, or corners, which are valuable and can be extended to various industrial applications such as signal transportation and energy trapping. To date, there have been fruitful methods to design various HOTIs such as quadrupole HOTIs [26], octupole HOTIs [27], and spinful HOTIs [28]. While by virtue of the straightforward concept and easy fabrication, designing by mimicking the Su-Schrieffer-Heeger (SSH) structure is one of the most popular methods to design HOTIs [29,30]. For example, Zhang *et al.* [31] drilled holes in a square lattice on a homogeneous rigid material and demonstrated the existence of robust topological

*chenzhenyu@seu.edu.cn
†bccwlim@cityu.edu.hk

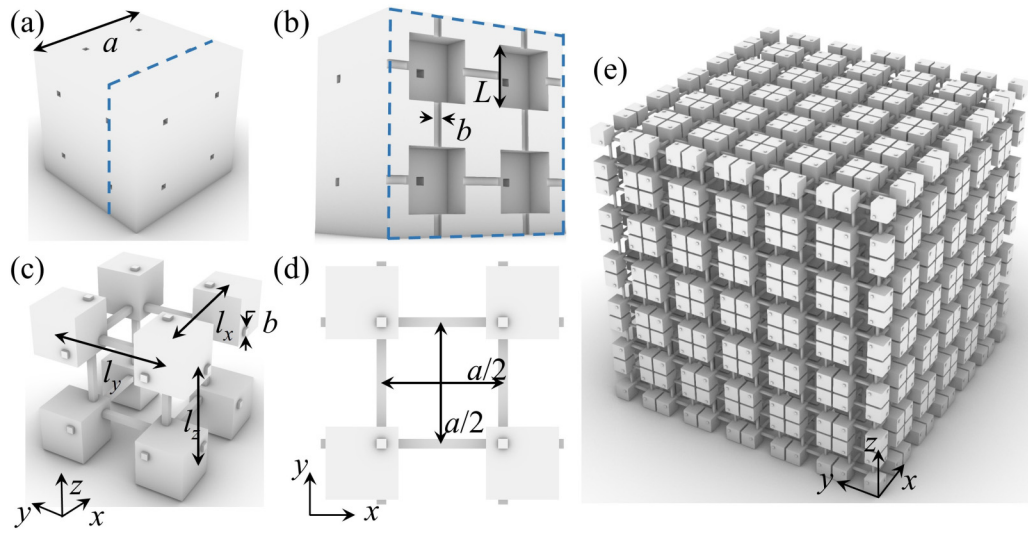

FIG. 1. The proposed 3D acoustic system with eight air cavities and the corresponding connecting channels. (a) 3D view of a unit cell, (b) cross-sectional view along the blue dashed frame, (c) 3D view of the extracted air domain in a unit cell, (d) plan of air domain in a unit cell, and (e) 3D view of the time domain for a finite structure.

corner states for spoof surface acoustic waves in this 2D second-order topological insulator (SOTI).

The majority of research on HOTIs today focuses on 2D structures with periodicity in two directions only [32–34]. In principle, 2D TIs only support the design of SOTIs at most, while the higher-order TIs, e.g., third-order topological insulators (TOTIs) can only be obtained using higher-dimensional TIs. Therefore, the exploration of 3D TIs has recently been a hot topic. In comparison to their 2D counterparts, 3D TIs offer one more degree of freedom in space for designing topological phases and thus broadening the scope and diversity of HOTIs. Theoretically, the 2D topological surface states, 1D topological hinge states, and 0D topological corner states can coexist in a 3D TOTI, which thus provides a versatile tool to manipulate light, vibration, and sound waves. For example, Xue *et al.* [35] designed a diamond lattice structure that consists of air cavities and interconnected air tubes, from which pressure concentration at structure corners can be observed. However, the present state-of-the-art for research related to TIs focuses on the presence of higher-order topological states and it is restricted to waveguiding in 2D space. The exploration of various wave propagation behavior, especially waveguiding in 3D space, is still in its infancy. In this paper, we fill the gap of research on the surface-, edge-, and corner-restricted wave propagation of 3D TIs by designing a cubic lattice structure with tunable topological order. In particular, the waveguiding in a 3D twisted path is successfully demonstrated, which is significant in sound wave manipulation and acoustic signal processing. A finite element approach using COMSOL is utilized to validate theoretical dispersion relation and wave propagation modes. Moreover, the proposed concept and model in this paper could be easily extended to future analogy research in elastic systems.

The rest of this paper is organized as follows. Section II elaborates on the analytical models and the specific geometrical parameters. It also introduces an equivalent electric circuit system for analyzing the dispersion relation. Section III presents a comprehensive study on directional bandgap and topological phases at different high-symmetry points. A fractional bulk polarization map is presented to illustrate topological phases in different directions. In Sec. IV, we first design a 1D first-order topological insulator (FOTI) to demonstrate the existence of topological edge states, and then the surface-restricted wave propagation is obtained in a 3D FOTI. Analogous examples of SOTIs and TOTIs are then presented in Secs. V and VI, respectively. Finally, we establish robust waveguiding with right-angle corners for both 2D and 3D twisted paths in Sec. VII.

II. MODEL AND METHODOLOGY

A. Modeling the acoustic metamaterials

To achieve a series of TIs with topological states along different directions and tunable order numbers, we herein propose an acoustic system with an analogy to the 3D SSH model. As shown in Fig. 1(a), the unit-cell model appearance is a sealed resin cube of side length a with four small ports on each surface. A cross section along the blue dashed frame is presented in Fig. 1(b) to show the internal structure. It is obvious that the model can be constructed by digging eight air cavities and the corresponding connecting channels from the resin cube. The air cavities are also cubic with side length L and air channel width b. For better illustration, we show the 3D view and the plan of extracted air domain in Figs. 1(c) and 1(d). The center-to-center distance of neighboring air cavities along the x, y, and z directions are respectively denoted as l_x, l_y, and l_z, while the air tube distance along any direction is fixed at $a/2$. It should be noticed that Figs. 1(a)–1(d) illustrate a unit cell, while the whole metastructure is a periodic repetition of the unit cell along the x, y, and z directions, as shown in Fig. 1(e). As an acoustic analogy of the 3D SSH model, the topological properties can be analyzed by the fractional bulk polarization $\mathbf{P}$ [36,37]. The respective air cavity distances i.e., $l_{x,y,z}$, are the tuning parameters for switching eigenmode

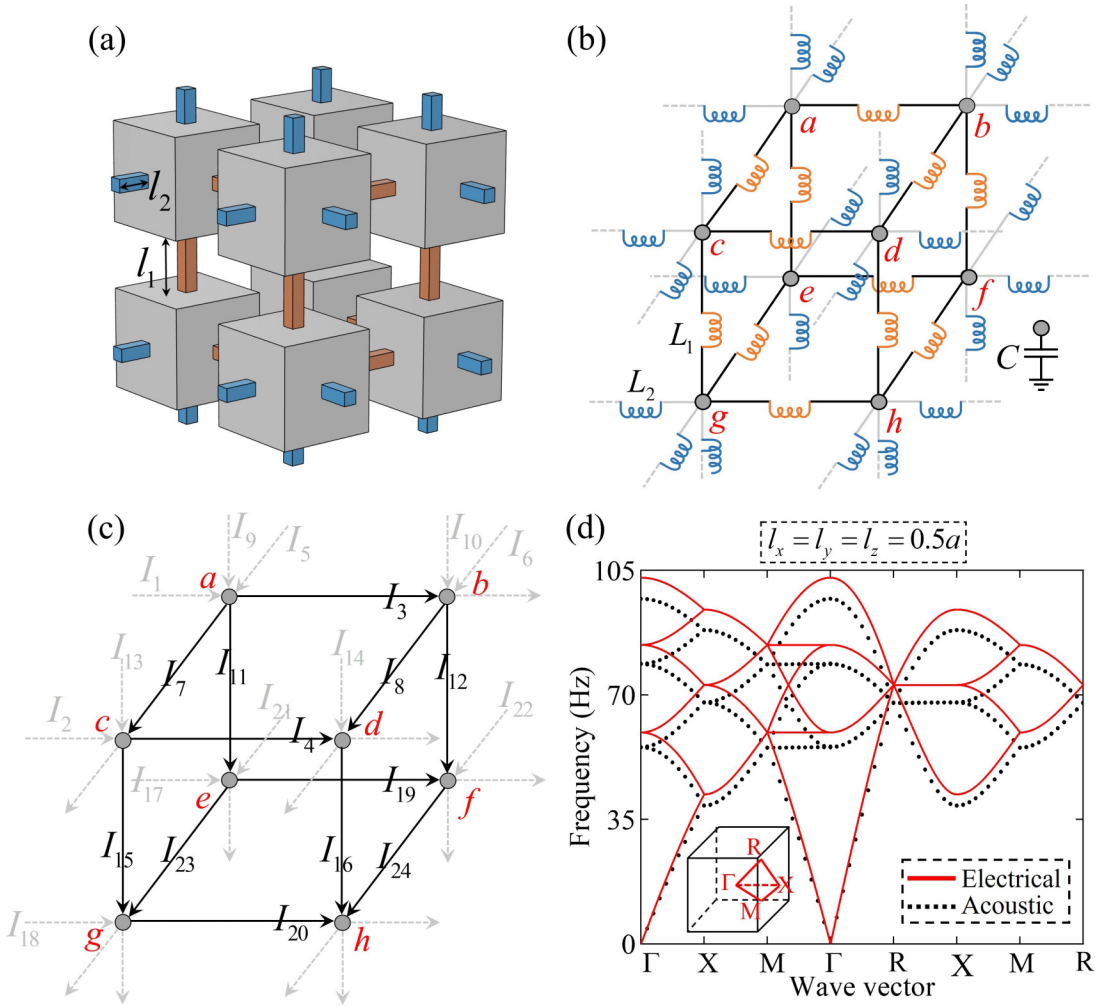

FIG. 2. Modeling of the equivalent electric system. (a) Air domain of unit cell with intracell air channels marked in orange and intercell air channels marked in blue. (b) Graphical illustration of the equivalent electric system, where inductors and ground-connected capacitors are electric counterparts of air channels and air cavities. (d) Schematic of currents I_1–I_{24} in the corresponding branches. (d) Comparison of dispersion relations for the acoustic system and the electric system with respect to $l_x = l_y = l_z = 0.5a$.

parity at the high-symmetry point of each direction, which will be discussed in detail in the following sections.

B. Equivalent electric circuit system

The proposed acoustic system has three degrees of freedom for tuning purposes, i.e., l_x, l_y, and l_z, such that switching of the eigenmode parity along different directions can be made possible. To avoid system complexity, we begin with an isotropic model i.e., $l_x = l_y = l_z$. As shown in Fig. 2(a), we can further categorize the air channels into intercell and intracell channels, respectively, marked in blue and orange. Considering the intricacy of the structure, it is difficult to directly derive an analytical dispersion relation of the acoustic system. Inspired by the topological electric system [38,39] and an analogy between electric systems and the proposed acoustic system [40–42], we introduce an equivalent electric system in Fig. 2(b) to analytically solve the band structure. According to Liao *et al.* [43], the gray cavities and blue (orange) channels in acoustic systems can be respectively equivalent to the ground-connected gray capacitors and blue (orange) serial inductors, of which the equivalent capacitance C and inductance L_2 (L_1) can be calculated by [41]

$$C = \frac{V}{\rho_0 c_0^2}, \quad L_i = \rho_0 \frac{l_i}{S}, \tag{1}$$

where l_i ($i = 1, 2$) represents the length of intracell (orange) channels or intercell (blue) channels, V denotes the volume of the air cavity, $\rho_0 = 1.21\ \mathrm{kg/m^3}$ is the air density, $c_0 = 343$ m/s is the sound velocity propagating in the air, and S is the cross-sectional area of the channels. The voltage and current in the electric system represent the pressure difference and volume flux in the acoustic system, respectively. In addition, the equivalence between the acoustic and electric systems has several limitations and assumptions, including (i) neglecting nonlinear material properties, (ii) neglecting viscosity, (iii) assuming the acoustic system is heat insulated, (iv) the wavelength of the acoustic wave must be significantly larger than the tube length i.e., l_x, l_y, and l_z, and (v) the volume of the cavities must be significantly larger than the tubes.

We first denote the current at each branch as I_i ($i = 1, 2, \ldots, 24$) with direction as indicated in Fig. 2(c), where the gray dashed arrows are intercell currents and the black solid arrows are intracell currents. Subsequently, by applying Kirchhoff's current law at nodes $a - h$, we obtain

$$I_1 + I_5 + I_9 = I_3 + I_{11} + I_7 + \frac{\partial}{\partial t} V_a C \tag{2a}$$

$$I_3 + I_6 + I_{10} = I_8 + I_{12} + I_1 e^{iq_x} + \frac{\partial}{\partial t} V_b C, \tag{2b}$$

$$I_2 + I_{13} + I_7 = I_4 + I_{15} + I_5 e^{iq_y} + \frac{\partial}{\partial t} V_c C, \tag{2c}$$

$$I_4 + I_{14} + I_8 = I_{16} + I_6 e^{iq_y} + I_2 e^{iq_x} + \frac{\partial}{\partial t} V_d C, \tag{2d}$$

$$I_{11} + I_{17} + I_{21} = I_{19} + I_{23} + I_9 e^{iq_z} + \frac{\partial}{\partial t} V_e C, \tag{2e}$$

$$I_{19} + I_{22} + I_{12} = I_{24} + I_{17} e^{iq_x} + I_{10} e^{iq_z} + \frac{\partial}{\partial t} V_f C, \tag{2f}$$

$$I_{18} + I_{23} + I_{15} = I_{20} + I_{21} e^{iq_y} + I_{13} e^{iq_z} + \frac{\partial}{\partial t} V_g C, \tag{2g}$$

$$I_{20} + I_{16} + I_{24} = I_{18} e^{iq_x} + I_{23} e^{iq_y} + I_{14} e^{iq_z} + \frac{\partial}{\partial t} V_h C. \tag{2h}$$

According to the current directions in Fig. 2(c) and the definition of voltage and current across an inductor $V = LdI/dt$, we may rewrite the equations above as

$$I_a = \left(\frac{3}{i\omega L_1} + \frac{3}{i\omega L_2} + i\omega C\right) V_a - \left(\frac{1}{i\omega L_1} + \frac{e^{-iq_x}}{i\omega L_2}\right) V_b - \left(\frac{1}{i\omega L_1} + \frac{e^{-iq_z}}{i\omega L_2}\right) V_e - \left(\frac{1}{i\omega L_1} + \frac{e^{-iq_y}}{i\omega L_2}\right) V_c, \tag{3a}$$

$$I_b = \left(\frac{3}{i\omega L_1} + \frac{3}{i\omega L_2} + i\omega C\right) V_b - \left(\frac{1}{i\omega L_1} + \frac{e^{iq_x}}{i\omega L_2}\right) V_a - \left(\frac{1}{i\omega L_1} + \frac{e^{-iq_z}}{i\omega L_2}\right) V_f - \left(\frac{1}{i\omega L_1} + \frac{e^{-iq_y}}{i\omega L_2}\right) V_d, \tag{3b}$$

$$I_c = \left(\frac{3}{i\omega L_1} + \frac{3}{i\omega L_2} + i\omega C\right) V_c - \left(\frac{1}{i\omega L_1} + \frac{e^{-iq_x}}{i\omega L_2}\right) V_d - \left(\frac{1}{i\omega L_1} + \frac{e^{-iq_z}}{i\omega L_2}\right) V_g - \left(\frac{1}{i\omega L_1} + \frac{e^{iq_y}}{i\omega L_2}\right) V_a, \tag{3c}$$

$$I_d = \left(\frac{3}{i\omega L_1} + \frac{3}{i\omega L_2} + i\omega C\right) V_d - \left(\frac{1}{i\omega L_1} + \frac{e^{iq_x}}{i\omega L_2}\right) V_c - \left(\frac{1}{i\omega L_1} + \frac{e^{-iq_z}}{i\omega L_2}\right) V_h - \left(\frac{1}{i\omega L_1} + \frac{e^{iq_y}}{i\omega L_2}\right) V_b, \tag{3d}$$

$$I_e = \left(\frac{3}{i\omega L_1} + \frac{3}{i\omega L_2} + i\omega C\right) V_e - \left(\frac{1}{i\omega L_1} + \frac{e^{-iq_x}}{i\omega L_2}\right) V_f - \left(\frac{1}{i\omega L_1} + \frac{e^{iq_z}}{i\omega L_2}\right) V_a - \left(\frac{1}{i\omega L_1} + \frac{e^{-iq_y}}{i\omega L_2}\right) V_g, \tag{3e}$$

$$I_f = \left(\frac{3}{i\omega L_1} + \frac{3}{i\omega L_2} + i\omega C\right) V_f - \left(\frac{1}{i\omega L_1} + \frac{e^{iq_x}}{i\omega L_2}\right) V_e - \left(\frac{1}{i\omega L_1} + \frac{e^{iq_z}}{i\omega L_2}\right) V_b - \left(\frac{1}{i\omega L_1} + \frac{e^{-iq_y}}{i\omega L_2}\right) V_h, \tag{3f}$$

$$I_g = \left(\frac{3}{i\omega L_1} + \frac{3}{i\omega L_2} + i\omega C\right) V_g - \left(\frac{1}{i\omega L_1} + \frac{e^{-iq_x}}{i\omega L_2}\right) V_h - \left(\frac{1}{i\omega L_1} + \frac{e^{iq_z}}{i\omega L_2}\right) V_c - \left(\frac{1}{i\omega L_1} + \frac{e^{iq_y}}{i\omega L_2}\right) V_e, \tag{3g}$$

$$I_h = \left(\frac{3}{i\omega L_1} + \frac{3}{i\omega L_2} + i\omega C\right) V_h - \left(\frac{1}{i\omega L_1} + \frac{e^{iq_x}}{i\omega L_2}\right) V_g - \left(\frac{1}{i\omega L_1} + \frac{e^{iq_z}}{i\omega L_2}\right) V_d - \left(\frac{1}{i\omega L_1} + \frac{e^{iq_y}}{i\omega L_2}\right) V_f. \tag{3h}$$

Here Eqs. (3a)–(3h) can be expressed into a matrix format as

$$\mathbf{I} = \mathbf{J}\mathbf{V}, \tag{4}$$

where $\mathbf{J}$ is the grounded Laplacian matrix with $\mathbf{J} = (i\omega\mathbf{C} + \mathbf{W}/i\omega)$ and

$$\mathbf{I} = [I_a \quad I_b \quad I_c \quad I_d \quad I_e \quad I_f \quad I_g \quad I_h]^T, \tag{5}$$

$$\mathbf{V} = [V_a \quad V_b \quad V_c \quad V_d \quad V_e \quad V_f \quad V_g \quad V_h]^T, \tag{6}$$

$$\mathbf{C} = \begin{bmatrix} C & 0 & \cdots & 0 & 0 \\ 0 & C & \cdots & 0 & 0 \\ \vdots & \ddots & \ddots & \ddots & \vdots \\ 0 & \cdots & \cdots & C & 0 \\ 0 & \cdots & \cdots & 0 & C \end{bmatrix}_{8\times 8}, \tag{7}$$

$$\mathbf{W} = \begin{bmatrix} \frac{3}{L_1} + \frac{3}{L_2} & -\frac{1}{L_1} - \frac{e^{-iq_x}}{L_2} & -\frac{1}{L_1} - \frac{e^{-iq_y}}{L_2} & 0 & -\frac{1}{L_1} - \frac{e^{-iq_z}}{L_2} & 0 & 0 & 0 \\ -\frac{1}{L_1} - \frac{e^{iq_x}}{L_2} & \frac{3}{L_1} + \frac{3}{L_2} & 0 & -\frac{1}{L_1} - \frac{e^{-iq_y}}{L_2} & 0 & -\frac{1}{L_1} - \frac{e^{-iq_z}}{L_2} & 0 & 0 \\ -\frac{1}{L_1} - \frac{e^{iq_y}}{L_2} & 0 & \frac{3}{L_1} + \frac{3}{L_2} & -\frac{1}{L_1} - \frac{e^{-iq_x}}{L_2} & 0 & 0 & -\frac{1}{L_1} - \frac{e^{-iq_z}}{L_2} & 0 \\ 0 & -\frac{1}{L_1} - \frac{e^{iq_y}}{L_2} & -\frac{1}{L_1} - \frac{e^{iq_x}}{L_2} & \frac{3}{L_1} + \frac{3}{L_2} & 0 & 0 & 0 & -\frac{1}{L_1} - \frac{e^{-iq_z}}{L_2} \\ -\frac{1}{L_1} - \frac{e^{iq_z}}{L_2} & 0 & 0 & 0 & \frac{3}{L_1} + \frac{3}{L_2} & -\frac{1}{L_1} - \frac{e^{-iq_x}}{L_2} & -\frac{1}{L_1} - \frac{e^{-iq_y}}{L_2} & 0 \\ 0 & -\frac{1}{L_1} - \frac{e^{iq_z}}{L_2} & 0 & 0 & -\frac{1}{L_1} - \frac{e^{iq_x}}{L_2} & \frac{3}{L_1} + \frac{3}{L_2} & 0 & -\frac{1}{L_1} - \frac{e^{-iq_y}}{L_2} \\ 0 & 0 & -\frac{1}{L_1} - \frac{e^{iq_z}}{L_2} & 0 & -\frac{1}{L_1} - \frac{e^{iq_y}}{L_2} & 0 & \frac{3}{L_1} + \frac{3}{L_2} & -\frac{1}{L_1} - \frac{e^{-iq_x}}{L_2} \\ 0 & 0 & 0 & -\frac{1}{L_1} - \frac{e^{iq_z}}{L_2} & 0 & -\frac{1}{L_1} - \frac{e^{iq_y}}{L_2} & -\frac{1}{L_1} - \frac{e^{iq_x}}{L_2} & \frac{3}{L_1} + \frac{3}{L_2} \end{bmatrix}. \tag{8}$$

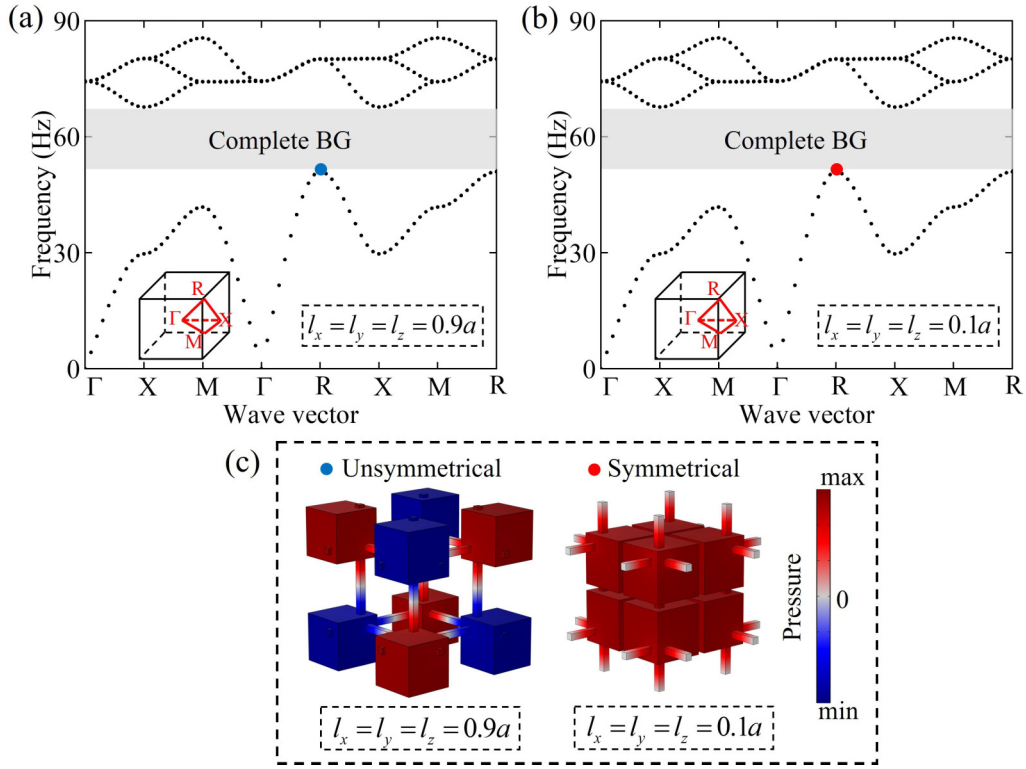

FIG. 3. Dispersion relation in the FBZ with respect to (a) $l_x = l_y = l_z = 0.9a$ and (b) $l_x = l_y = l_z = 0.1a$, where the diagram of the FBZ is shown in the inset. (c) Eigenmodes of both cases at a higher symmetry point R for the first band.

According to Kirchhoff's current law, the current vector $\mathbf{I}$ must be a zero vector. Therefore, by assuming the voltage at each node that varies in the form of $\mathbf{V} = \boldsymbol{\phi} e^{i\omega t}$, we can rewrite the grounded Laplacian matrix as

$$\mathbf{W}\boldsymbol{\phi} = \omega^2 \mathbf{C}\boldsymbol{\phi}. \tag{9}$$

After introducing a gauge transformation $\bar{\boldsymbol{\phi}} = \mathbf{C}^{-1/2}\boldsymbol{\phi}$ and $\mathbf{D} = \mathbf{C}^{-1/2}\mathbf{W}\mathbf{C}^{-1/2}$, Eq. (8) can be further expressed in the following form:

$$\mathbf{D}\bar{\boldsymbol{\phi}} = \omega^2 \bar{\boldsymbol{\phi}}. \tag{10}$$

By determining eigenvalues of the dynamical matrix $\mathbf{D}$, one can obtain the dispersion relation of the equivalent electric circuit system.

To validate the equivalent electrical system, we further compare the dispersion solution from Eq. (10) with the finite element method (FEM) result of acoustic system solved using COMSOL MULTIPHYSICS. At an initial state, the geometrical parameters are defined as $a = 1$ m, $L = 0.3a$, $b = 0.04a$, and $l_x = l_y = l_z = 0.5a$. As shown in Fig. 2(d), the dispersion relation in the first Brillouin zone (FBZ), highlighted as a red pyramid, is sufficient for analysis because of system periodicity. As observed, the equivalent electrical system (red solid line) and acoustic system (black dashed line) show satisfactory agreement. Taking the high-symmetry point R as an example, the analytical and numerical solutions are, respectively, 72.6 and 68.7 Hz, with a 5.4% difference, which is acceptable. Moreover, obvious degeneracy characteristics resulting from the system symmetry can be observed. The structure owns four eigenmodes at the Γ point while it degenerates into three, two, and one eigenmode at points X, M, and R, respectively.

III. UNIT-CELL ANALYSIS

A. Isotropic unit cells

A unit cell with identical intra- and intercell coupling, i.e., $l_1 = l_2$ presents a continuous dispersion relation with obvious degeneracy characteristics in Fig. 2(d). In this section, we retain an isotropic structure where $l_x = l_y = l_z$, but introduce distinct intra- and intercell coupling, i.e., $l_1 \neq l_2$. Two cases with $l_x = l_y = l_z = 0.9a$ and $l_x = l_y = l_z = 0.1a$ are investigated, of which the dispersion relations are respectively shown in Figs. 3(a) and 3(b). Because this paper focuses on subwavelength scale and analyzes higher-order topology, only the lowest bandgap and its corresponding topological properties will be investigated, although high-frequency bandgaps do exist. After setting $l_1 \neq l_2$, the degeneracy of the first two bands is lifted so that a complete bandgap ranging from 50.93 to 69.95 Hz occurs. It can be observed that these two cases show identical bandgap ranges but with distinct eigenmodes at a higher symmetry point R. As shown in Fig. 3(c), $l_x = l_y = l_z = 0.9a$ corresponds to an eigenmode that is symmetric along neither the xz, xy, nor the yz plane, nor is it denoted as an unsymmetric mode (marked by blue cycle). By contrast, the eigenmode for $l_x = l_y = l_z = 0.1a$ (marked by red cycle) is symmetric about the xz, yz, and xy planes. The changing of eigenmodes suggests this structure can achieve topological phase transition from nontrivial to trivial by simply tweaking the air cavity distance. For isotropic cases, the symmetry along any plane is promised to be identical to the $Pm3m$

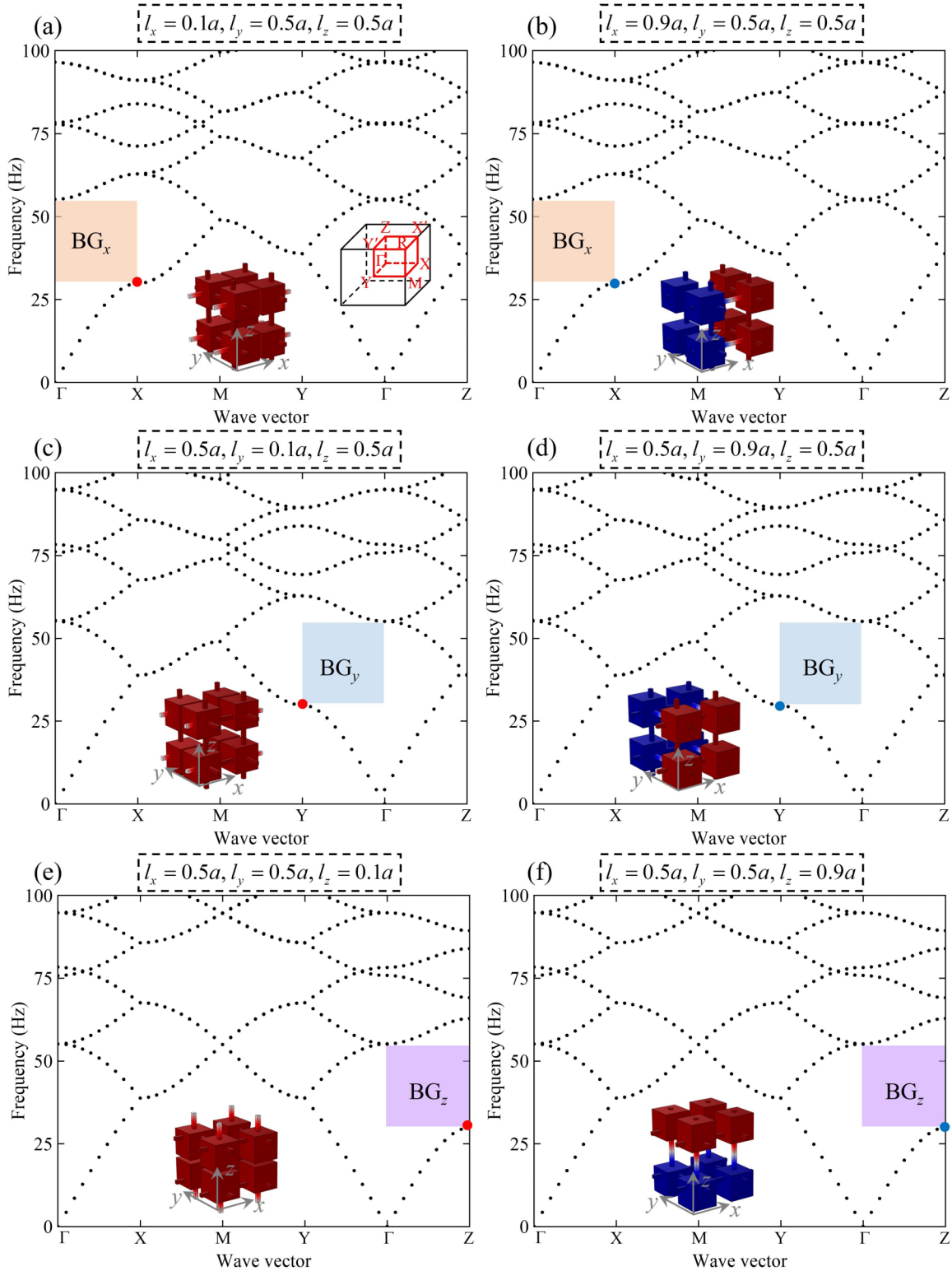

FIG. 4. Dispersion relation along Γ-*X*-*M*-*Y*-Γ-*Z* for (a) $l_x = 0.1a$, $l_y = 0.5a$, $l_z = 0.5a$; (b) $l_x = 0.9a$, $l_y = 0.5a$, $l_z = 0.5a$; (c) $l_x = 0.5a$, $l_y = 0.1a$, $l_z = 0.5a$; (d) $l_x = 0.5a$, $l_y = 0.9a$, $l_z = 0.5a$; (e) $l_x = 0.5a$, $l_y = 0.5a$, $l_z = 0.1a$; and (f) $l_x = 0.5a$, $l_y = 0.5a$, $l_z = 0.9a$, where the Brillouin zone and eigenmodes at the corresponding higher symmetry points are shown in the insets.

symmetry (threefold rotation symmetry and three mirror symmetries) of this cubic SSH lattice. Therefore, the eigenmodes are either symmetrical or unsymmetrical along all planes.

B. Anisotropic unit cells

From the analysis of isotropic unit cells in Sec. III A, it is obvious that a complete bandgap could be opened by

tweaking the cavities distance, and the eigenmodes show identical symmetry properties about all planes i.e., either symmetrical or unsymmetrical. In this section, anisotropy is introduced to the 3D SSH acoustic system, and the directional bandgaps and the corresponding topological properties are analyzed. To begin with, it is significant to emphasize the dispersion relation along Γ-X-M-Y-Γ-Z [see the red box inserted in Fig. 4(a)] is used in this section instead of adopting the FBZ [see the red pyramid in Fig. 3(a)], such that the directional bandgaps can be clearly observed. Two anisotropic cases, $l_x = 0.9a$ and $l_x = 0.1a$ with $l_y = l_z = 0.5a$, are first studied to demonstrate the x-direction bandgap. As shown in Figs. 4(a) and 4(b), the degeneracy at the X point is lifted because of the unequal intracell and intercell coupling along the x direction. Comparatively, the degeneracy of other points is preserved, hence the bandgap denoted as BG_x only occurs along the ΓX direction, the frequency ranges of which are identical. However, by observing the eigenmodes of the first band at the X point, reversing of the symmetry about the yz plane is noticed by changing l_x from $0.9a$ to $0.1a$. It is interesting to highlight that the symmetry property along the other two planes, i.e., the xz and xy planes, are not affected. An analogous analysis for the y and z directions are also performed and the result is presented in Figs. 4(c) and 4(d) and Figs. 4(e) and 4(f). It can be concluded from Fig. 4 that the opening or closing of bandgaps in the ΓX, ΓY, and ΓZ directions only depends on l_x, l_y, and l_z, respectively. Moreover, topological phase transition follows the same configuration, which means the symmetry property about the yz, xz, and xy planes is independently related to l_x, l_y, and l_z. This property provides possibilities for designing different order TIs that are polarized along different directions.

C. Fractional bulk polarization

The previous analysis for isotropic and anisotropic unit cells demonstrates the dependence of the type of eigenmode on air cavity distance. Topological phase transition in a specific direction can be observed. Here, we introduce 3D fractional bulk polarization $\mathbf{P} = (P_x, P_y, P_z)$ to characterize the topological properties. Note that some researchers employ Zak phase $\theta_i^{\mathrm{Zak}} (i = x, y, z)$ to describe topological properties [44,45], which is actually related to bulk polarization with $P_i = \theta_i^{\mathrm{Zak}}/2\pi$. The 3D fractional bulk polarization is defined as the integral of Berry connection over the FBZ [46,47]

$$\mathbf{P} = \frac{1}{(2\pi)^3} \int\int\int_{\mathrm{FBZ}} d^3\mathbf{k}\, \mathrm{Tr}(\mathbf{A}_n), \quad \mathbf{A}_n = i\langle u_n|\partial_{\mathbf{k}}|u_n\rangle, \quad (11)$$

where $\mathbf{k}$ is the wavevector, $\partial_{\mathbf{k}}$ is the vector gradient operator in $\mathbf{k}$ space, $|u_n\rangle$ is the Bloch function, and subscript n refers to the nth bands below the bandgap. It should be noted that the band index n is equal to 1 in this study because we only focus on the lowest bandgap. The bulk polarization is identical along all directions for isotropic unit cells, i.e., $P_x = P_y = P_z$, since the crystalline symmetry is preserved. Comparatively, distinct bulk polarization values can be obtained for anisotropic unit cells. It is rather difficult to determine $\mathbf{P}$ from Eq. (11) directly. Determining the polarization P_i $(i = x, y, z)$ from parities of eigenmodes at the corresponding higher symmetry points is preferred [48,49].

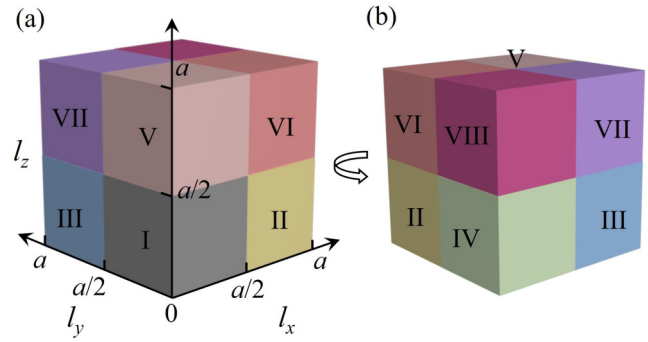

FIG. 5. Fractional bulk polarization map that indicates the relation between the topological phase and air cavities distance, i.e., l_x, l_y, and l_z. (a) Isometric map and (b) different isometric map with (a) but with 180 ° rotation about the l_z axis.

$$P_i = \frac{1}{2}\left(\sum_n q_i^n \bmod 2\right), \quad (-1)^{q_i^n} = \frac{\eta_n(D_i)}{\eta_n(\Gamma)}, \quad (12)$$

where D_i $(i = x, y, z)$ represent higher symmetry points along the x, y, and z directions, respectively, i.e., $D_x = X[\mathbf{k} = (\pi/a, 0, 0)]$, $D_y = Y[\mathbf{k} = (0, \pi/a, 0)]$, and $D_z = Z[\mathbf{k} = (0, 0, \pi/a)]$. η_n $(n = 1)$ refers to parity of the first band, where symmetric eigenmodes give even $(+)$ parity and unsymmetrical modes give odd $(-)$ parity. It should be noticed the reference plane for symmetry estimation differs with directions. For example, we take the yz plane for reference when estimating the symmetry property for D_x, and the xz (xy) plane is selected for D_y (D_z). Therefore, the bulk polarization P_i is 0 (1/2) if the eigenmodes of the first band at the corresponding higher symmetry point are symmetric (unsymmetrical).

To establish the whole relation between cavity distance l_i and $\mathbf{P}$ values, we further conduct a series of parametric studies and summarize the bulk polarization map in Fig. 5 and Table I. Based on l_i, we divide the bulk polarization map

TABLE I. Details of color and bulk polarization with respect to regions I–VIII.

Region	Color	Bulk polarization value
I		$\mathbf{P} = (0, 0, 0)$
II		$\mathbf{P} = (1/2, 0, 0)$
III		$\mathbf{P} = (0, 1/2, 0)$
IV		$\mathbf{P} = (1/2, 1/2, 0)$
V		$\mathbf{P} = (0, 0, 1/2)$
VI		$\mathbf{P} = (1/2, 0, 1/2)$
VII		$\mathbf{P} = (0, 1/2, 1/2)$
VIII		$\mathbf{P} = (1/2, 1/2, 1/2)$

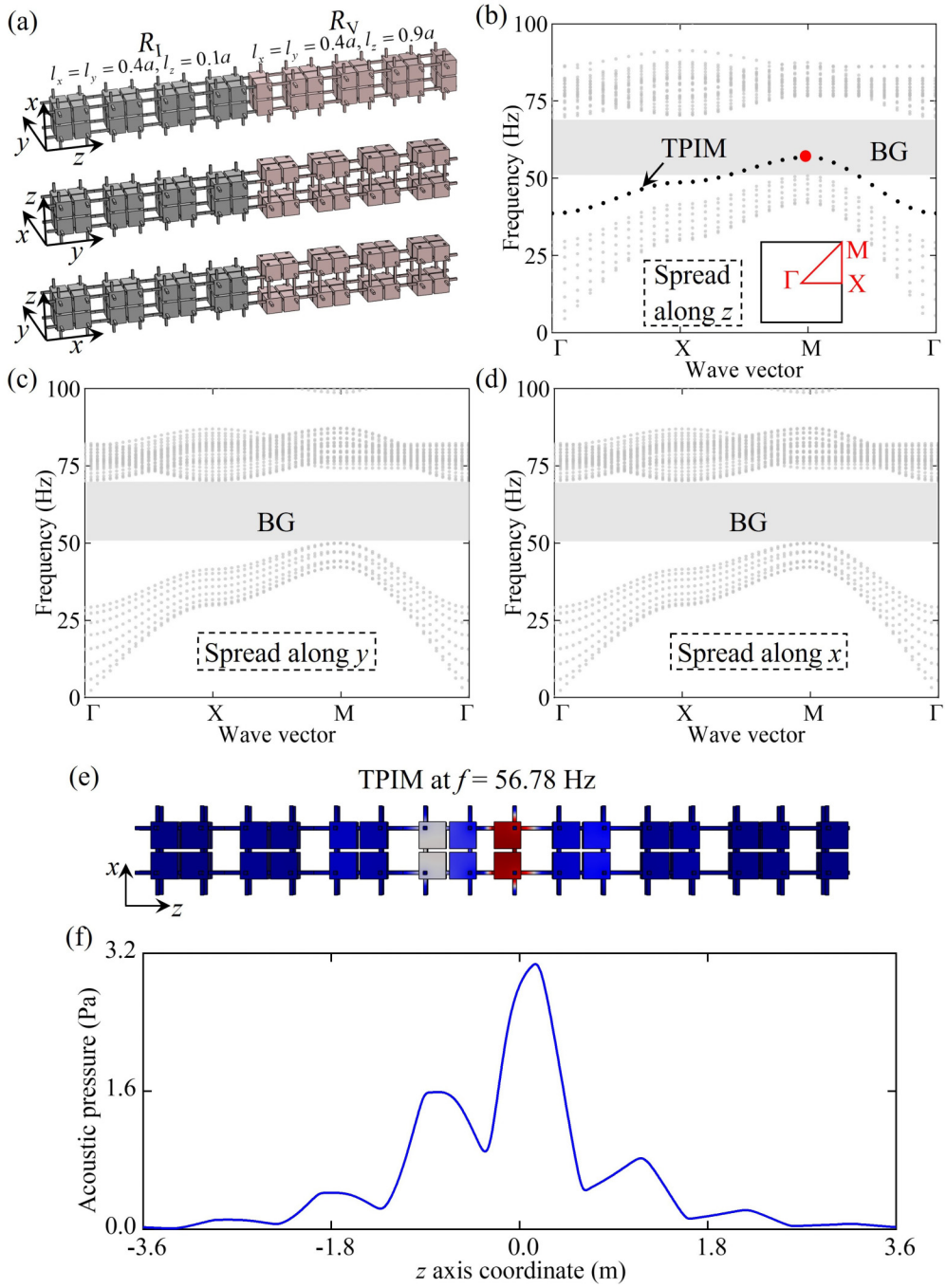

FIG. 6. Dispersion analysis of 1D FOTIs. (a) 1D FOTIs with unit cells spreading along the z, y, and x direction, respectively. (b)–(d) correspond to dispersion relations in the 2D FBZ. (e) Mode shape of the TPIM for the FOTI that spreads along the z direction. (f) Acoustic pressure distribution along the z direction for the eigenmodes in (e).

into eight regions that are denoted by R_{I}-R_{VIII} and marked by different colors. Every region has its unique color and bulk polarization value. It can be concluded from Fig. 5 and Table I that P_i is only related to the corresponding l_i. For example, P_y is promised to be 0 (1/2) only if $l_y < a/2$ ($l_y > a/2$), while l_x and l_z are insignificant, which agrees well with our conclusion in Fig. 4. Such properties offer a clear strategy for obtaining different order or directional topological phases in a parametric space.

IV. FOTI

A. One-dimensional FOTI

The dispersion relation analyses in the previous sections demonstrated controllable directional bandgap and topological phase transition. Here, we propose three 1D FOTIs to establish the directional TPIM. According to bulk-boundary correspondence [30,50], a TPIM along one specific direction can be formed at the interface of two domains with common

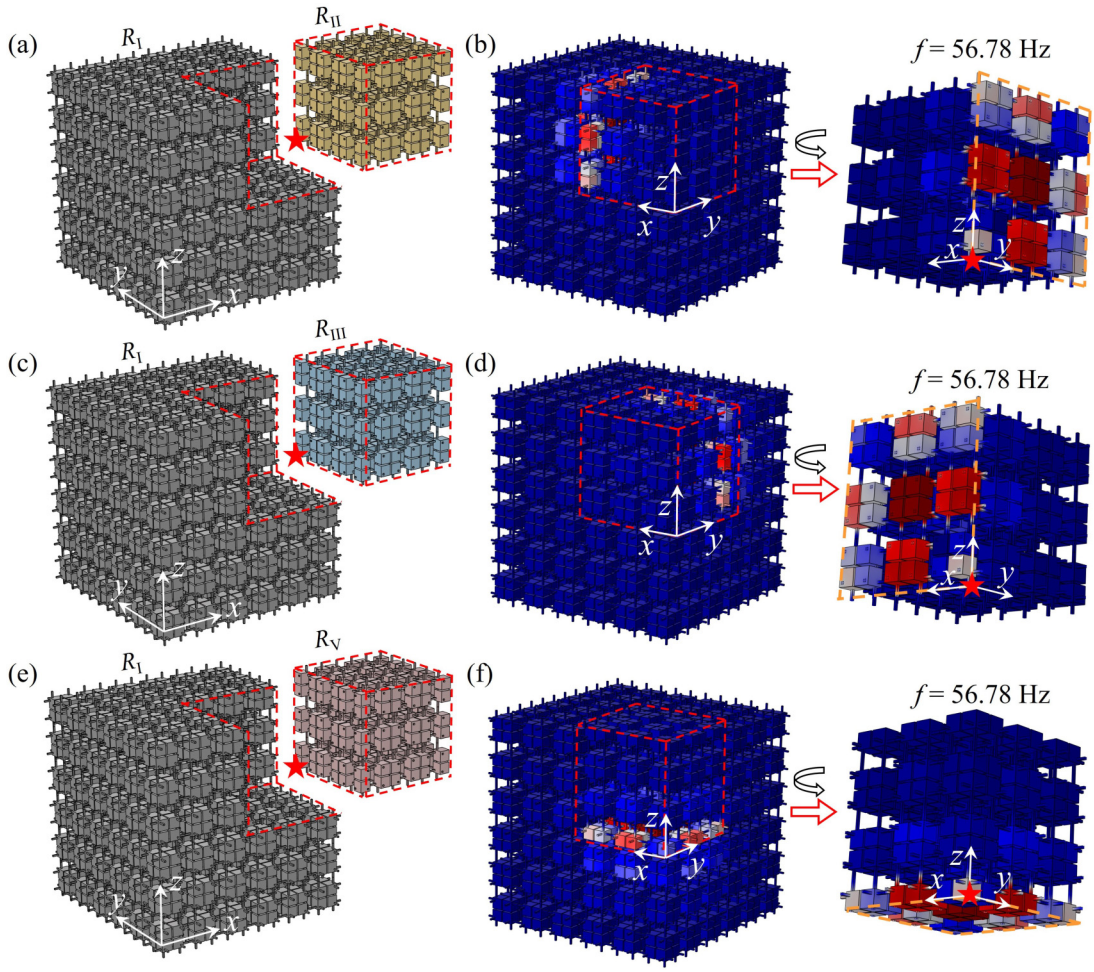

FIG. 7. Wave propagation analysis of 3D FOTIs. (a) Schematic diagram and (b) surface-restricted yz plane waveguiding at $f = 56.78$ Hz of the 3D FOTI with R_{I} unit cells and R_{II} unit cells. (c) Schematic diagram and (d) surface-restricted xz plane waveguiding at $f = 56.78$ Hz of the 3D FOTI with R_{I} unit cells and R_{III} unit cells. (e) Schematic diagram and (f) surface-restricted xy plane waveguiding at $f = 56.78$ Hz of the 3D FOTI with R_{I} unit cells and R_{V} unit cells.

bandgap regions but opposite topological phases along that specific direction. Therefore, three supercells in Fig. 6(a) that are composed of four R_{I} and four R_{V} unit cells but spread along different directions are designed. The first supercell spreads along the z direction and periodic boundary conditions (PBCs) are applied to the other two directions. The other two supercells follow analogous configurations. The dispersion relations are presented in Figs. 6(b)–6(d) by sweeping the wave vector along the 2D FBZ [see the red triangle in Fig. 6(b)]. It is obvious that a TPIM only occurs for the supercell spreading along z, since R_{I} [$\mathbf{P} = (0, 0, 0)$] and R_{V} [$\mathbf{P} = (0, 0, 1/2)$] unit cells only provide a z-direction phase transition. Unlike gapless TPIMs in (spin) Chern insulators [1,51], this structure exhibits a gapped TPIM band, which predicts the existence of higher-order topological insulators. The sound pressure field of the TPIM at 56.78 Hz is shown in Fig. 6(e), from which we can notice pressure localization at the interface. As PBCs are applied to the x and y directions, we can promise the existence of sound wave propagation along the xy plane for a 3D FOTI, which will be investigated in the following section. Moreover, it can also be quantitatively observed from Fig. 6(f) that the acoustic pressure is much higher around the interface, and it decays rapidly away from it. The pressure is attenuated to near zero within $1.5a$ from the interface.

B. Three-dimensional FOTI

The analysis in Sec. IV A predicts the presence of surface-restricted wave propagation in 3D FOTIs. Due to single-directional phase conflict and PBCs along the other directions, a 3D FOTI with different P_z components should have xy surface-restricted wave propagation and vice versa. Therefore, three kinds of 3D FOTI, as inserted in Figs. 7(a), 7(c), and 7(e), are designed to verify the prediction. Taking Fig. 7(a) as an example, the structure is composed of $6\times6\times6$ unit cells, where the nontrivial (yellow) parts are R_{II} [$\mathbf{P} = (1/2, 0, 0)$] unit cells and the others are trivial R_{I} [$\mathbf{P} = (0, 0, 0)$] unit cells. Note that the R_{I} and R_{II} parts are interconnected with no gap, but we split them in the diagram for better presentation. By setting a 56.78 Hz point excitation at the connecting corners (red star) between R_{I} and R_{II} parts, we obtain the wave propagation mode in Fig. 7(b), where an R_{II} pressure field is shown independently. It can be seen the

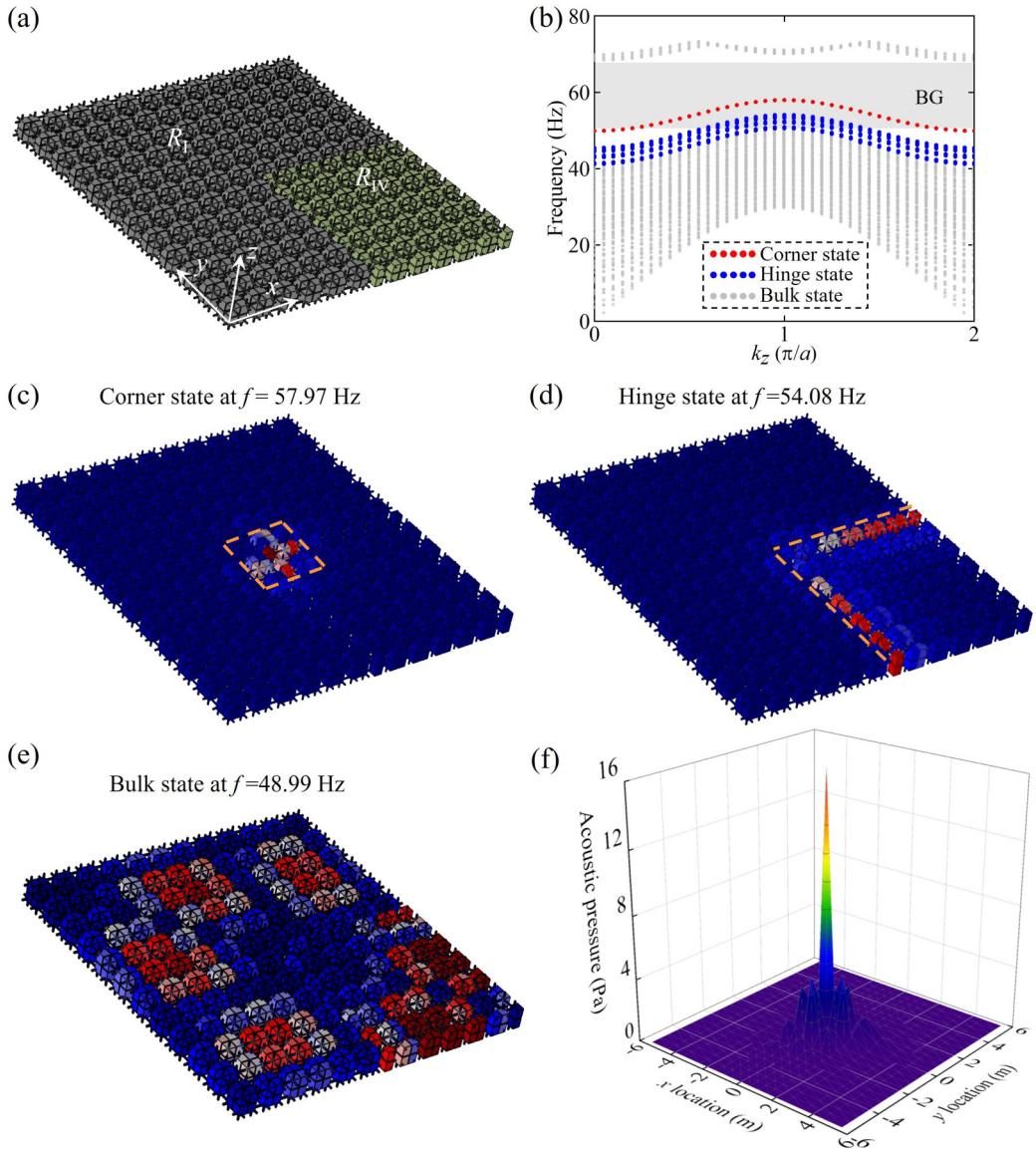

FIG. 8. Dispersion analysis of 2D SOTIs. (a) Schematic diagram and (b) dispersion relation of a 2D SOTI with unit cells spreading along the x and y directions. Eigenmodes of (c) one topological corner state at $f = 57.97$ Hz; (d) one topological hinge state at $f = 54.08$ Hz; (e) one bulk state at $f = 48.99$ Hz; and (f) acoustic pressure distribution for the corner state at $f = 57.97$ Hz.

56.78 Hz sound wave propagates strictly along the intersurface of the yz plane. Together with the analogous phenomenon for the xz plane [inserted in Figs. 7(c) and 7(d)] and the xy plane [inserted in Figs. 7(e) and 7(f)], we successfully demonstrate the surface-restricted wave propagation along different planes in the 3D FOTIs. The wave propagation plane can be easily switched by tweaking the cavities distance i.e., l_x, l_y, and l_z. With the ability to confine wave propagation in a specific plane, this new model shows great application potential in structural damage detection [52] and wave filtering [53].

V. SOTI

A. Two-dimensional SOTI

In Sec. IV, TPIMs and the corresponding surface-restricted wave propagation of FOTIs are established using unit cells with single-directional phase conflict. According to bulk-boundary correspondence, the dual-directional topological phase conflict is able to generate lower-order topological states at the "boundary of boundary" because of convergence of two orthometric 1D interface polarization. The so-called "bulk-boundary-corner" correspondence is defined by a topological corner charge as [54]

$$Q_{\rm corner} = P_i P_j \ (i, j = x, y, z \text{ and } i \neq j), \tag{13}$$

where a nonzero $Q_{\rm corner}$ can ensure the presence of topological corner states. A 90° terminated corner is necessary for obtaining corner states, hence a 1D SOTI is theoretically nonexistent. As shown in Fig. 8(a), we design a 2D SOTI with 12×12 unit cells whose right bottom quarter (green part) belongs to $R_{\rm IV}$ [$\mathbf{P} = (1/2, 1/2, 0)$] and the other parts belong to $R_{\rm I}$ [$\mathbf{P} = (0, 0, 0)$]. Since phase conflict originates from P_x

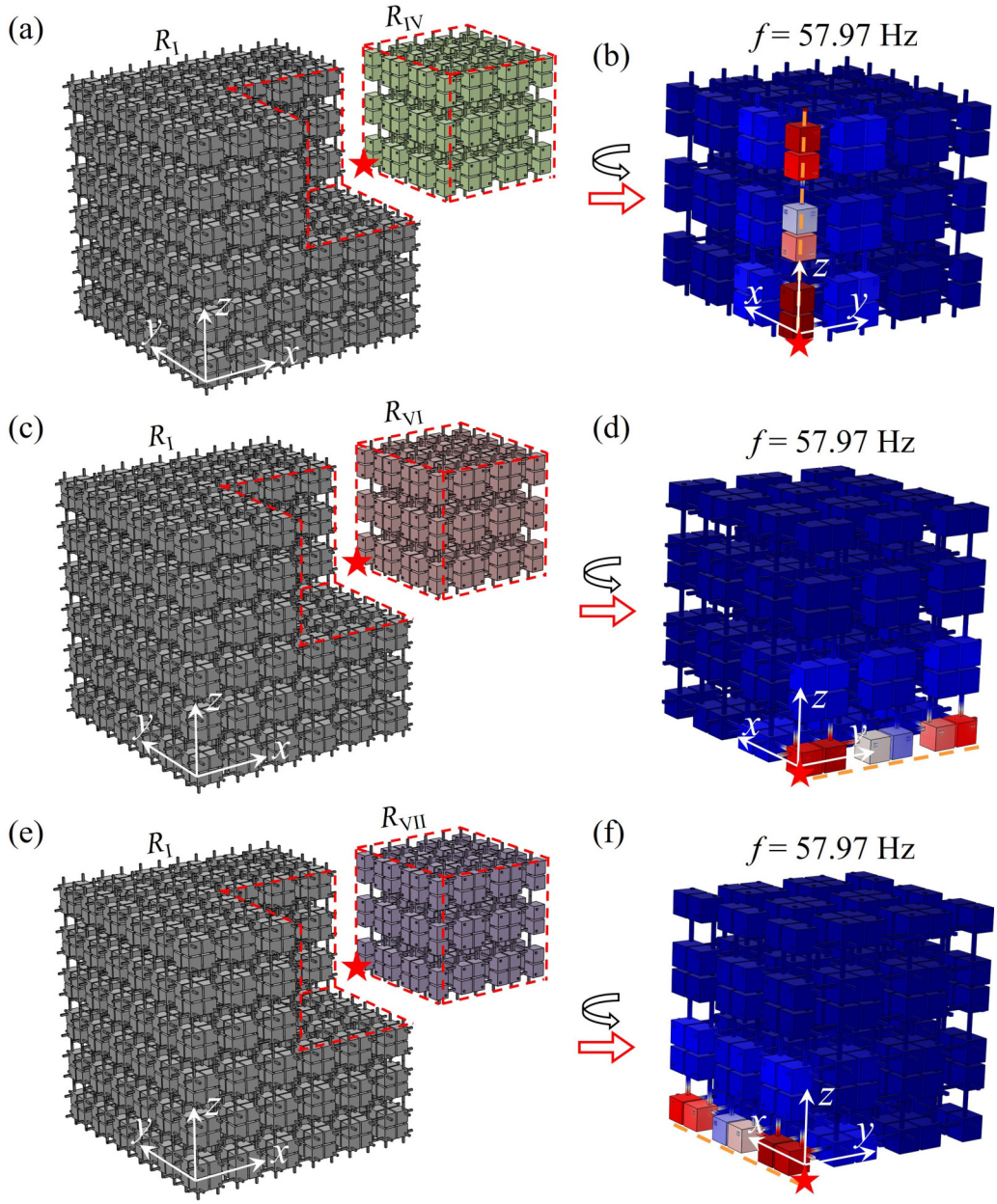

FIG. 9. Wave propagation analysis of 3D SOTIs. (a) Schematic diagram and (b) edge-restricted z-directional waveguiding at $f = 57.97$ Hz of the 3D SOTI that is composed of R_{I} unit cells and R_{IV} unit cells. (c) Schematic diagram and (d) edge-restricted y-directional waveguiding at $f = 57.97$ Hz of the 3D SOTI that is composed of R_{I} unit cells and R_{VI} unit cells. (e) Schematic diagram and (f) edge-restricted x-directional waveguiding at $f = 57.97$ Hz of the 3D SOTI that is composed of R_{I} unit cells and R_{VII} unit cells.

and P_y, we spread the unit cells along the x and y directions and apply a PBC to the z direction. The dispersion can thus be solved by only sweeping the z-direction wave vector k_z. As shown in Fig. 8(b), the hinge states (blue dots) and corner states (red dots) occur in the bulk bandgap range (gray region). More specifically, the pure corner states only occupy 54.09–57.97 Hz, while the hinge states and corner states coexist from 49.89 to 54.09 Hz. Moreover, there is a frequency range above corner states, i.e., 57.97–68.34 Hz, in which all propagation modes are prohibited. This frequency range is referred to as a complete bandgap. The eigenmodes of one corner state, one hinge state, and one random bulk state are respectively shown in Figs. 8(c)–8(e). It can be observed the acoustic pressure in the hinge states localizes at the two orthometric interboundaries between the R_{I} and R_{IV} parts. Then, we can notice the dimensional hierarchy from hinge states to corner states. In Fig. 8(c), the acoustic pressure is highly confined at the boundary of boundary, which is a corner. It is easy to imagine that the corner in the 2D plane could be extended to a line in the 3D space, hence edge-restricted wave propagation can be achieved. Comparatively, the acoustic pressure is distributed throughout the whole structure in bulk states, which suggests free propagation of the sound wave. Moreover, the pressure map of corner states is presented in Fig. 8(f) for a quantitative analysis of the pressure distribution. It can be noticed pressure is localized around the center and it decays rapidly from it.

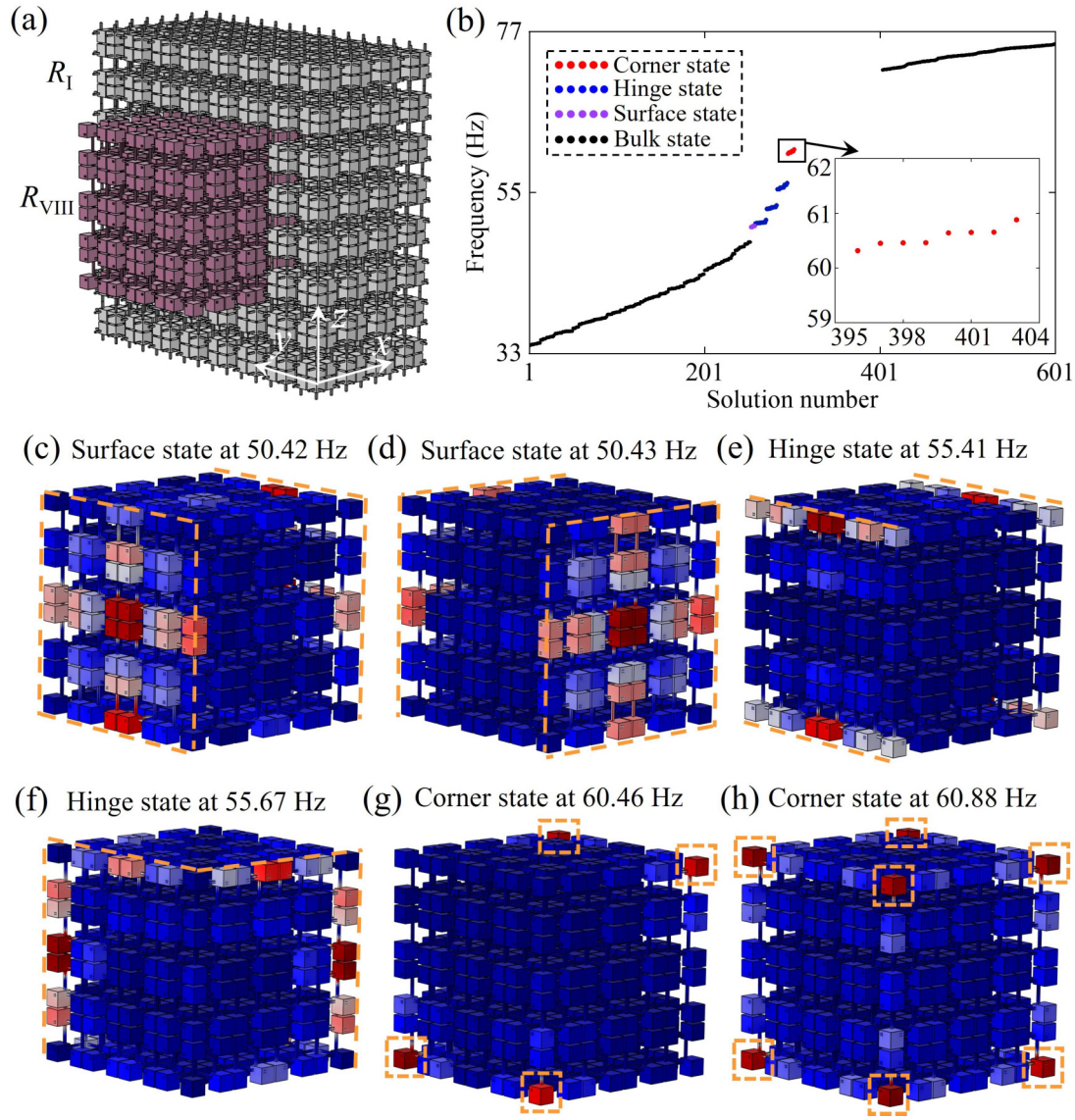

FIG. 10. Eigenfrequency analysis of 3D TOTI. (a) Schematic diagram of the proposed 3D TOTI that is composed of $4 \times 4 \times 4$ R_{VIII} unit cells and surrounded by two layers of R_{I} unit cells. (b) Eigenfrequencies and corresponding solution numbers. Eigenmodes of (c),(d) two topological surface states at $f = 50.42$ Hz and $f = 50.43$ Hz, (e),(f) two topological hinge states at $f = 55.41$ Hz and $f = 55.67$ Hz, and (g),(h) two topological corner states at $f = 60.46$ Hz and $f = 60.88$ Hz.

The pressure approaches zero at the location about $1.5a$ away from center.

B. Three-dimensional SOTI

In Sec. IV, the surface-restricted wave propagation is obtained in 3D FOTIs, while in Sec. V A, we show the lower-dimensional energy localization (corner state) in SOTI. Therefore, it is natural to think whether edge-restricted wave propagation can be obtained in higher-order topological insulators. As shown in Figs. 9(a), 9(c), and 9(e), we propose three kinds of 3D SOTIs that are analogous to the structure in Fig. 7 but the nontrivial region has different bulk polarization. For SOTIs, the dual-directional phase conflict should be ensured, hence we chose R_{I} as the trivial part and R_{IV}, R_{VI}, and R_{VII} as the nontrivial part, respectively. Taking Fig. 9(a) as an example, the bulk polarization of green (R_{IV}) parts and gray (R_{I}) parts are respectively $\mathbf{P} = (1/2, 1/2, 0)$ and $\mathbf{P} = (0, 0, 0)$. Then, the edge-restricted wave propagation along the z direction is obtained by giving a 57.97 Hz excitation at the interconnetcing corner (red star), as depicted in Fig. 9(b). By using the same analysis approach, we demonstrate wave propagation along the y and x edges in Figs. 9(d) and 9(f).

VI. TOTI

In the previous sections, a FOTI with single-directional phase conflict and a SOTI with dual-directional phase conflict have demonstrated the topological 1D interface states, 2D hinge states, 2D corner states, and the corresponding surface-restricted and edge-restricted wave propagation modes. The higher-order cases will be discussed in this section. Based on the definition of 3D corner charge ($Q_{\mathrm{corner}} = P_x P_y P_z$), the 3D corner states can be ensured by nonzero bulk

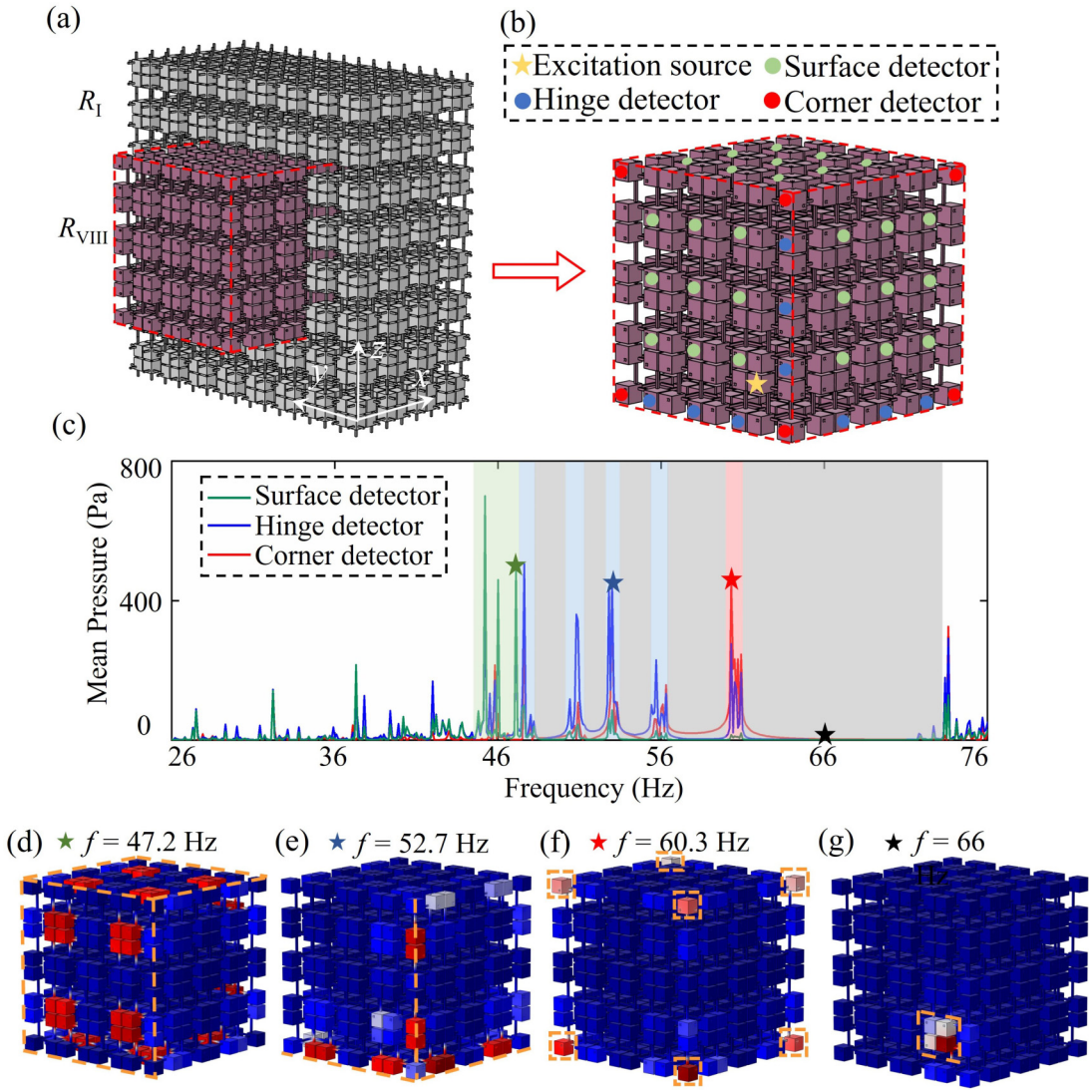

FIG. 11. Wave propagation analysis of the 3D TOTI. (a) Schematic diagram of the proposed 3D TOTI. (b) Installation layout of the excitation source, corner detectors, hinge detectors, and surface detectors. (d) Mean pressure obtained by different detectors with respect to the excitation frequency from 26 to 76 Hz. Wave propagation behavior of (d) $f = 47.2$ Hz that belongs to the surface states region, (e) $f = 52.7$ Hz that belongs to the hinge states region, (f) $f = 60.3$ Hz that belongs to the corner states region, and (g) $f = 66$ Hz that belongs to the bandgap region.

polarization along three directions simultaneously. Moreover, it can be observed from Fig. 5 and Table I that there exist two regions with triple-directional phase conflict, e.g., R_{I} [$\mathbf{P} = (0, 0, 0)$] and R_{VIII} [$\mathbf{P} = (1/2, 1/2, 1/2)$]. Therefore, we propose a TOTI [inserted in Fig. 10(a)], which consists of $4 \times 4 \times 4$ R_{VIII} unit cells surrounded by two layers of R_{I} unit cells. The eigenfrequencies and corresponding solution numbers of this structure are solved and presented in Fig. 10(b). As predicted, several surface states, hinge states, and corner states take place in the bulk gap range, which are respectively marked by purple, blue, and red dots. In principle, the number of corner states depends on the number of interconnected corners. As a cubic structure, the proposed model has eight corners that match well with the corner states number [see the inserted local plot in Fig. 10(b)]. Two eigenmodes of each state are shown in Figs. 10(c)–10(h), where only the pressure field of R_{I} parts is presented for a clearer presentation. It is obvious the sound pressure is restricted on the surfaces but insulated in the bulk for surface states. By contrast, the pressure concentrates at a lower-dimensional geometry (edge) for topological hinge states and it decays rapidly into surface and bulk. For the eigenmodes of red dots, it can be noticed the pressure is discretely confined at the corners but insulated for either edge, surface, or bulk, which is a smoking gun of topological corner states. By solving eigenmodes of the proposed structure, the presence of topological corner states is successfully demonstrated. However, the actual wave propagation behavior in this 3D SOTI is still unclear.

After eigenmode analysis, we further conduct a frequency domain study to investigate the wave propagation behavior of 3D TOTI. As shown in Fig. 11(a), the model is completely identical to that in Fig. 10(a), but instead of solving eigenmodes, we give a sound excitation and observe the frequency response. The source and detector installation locations are

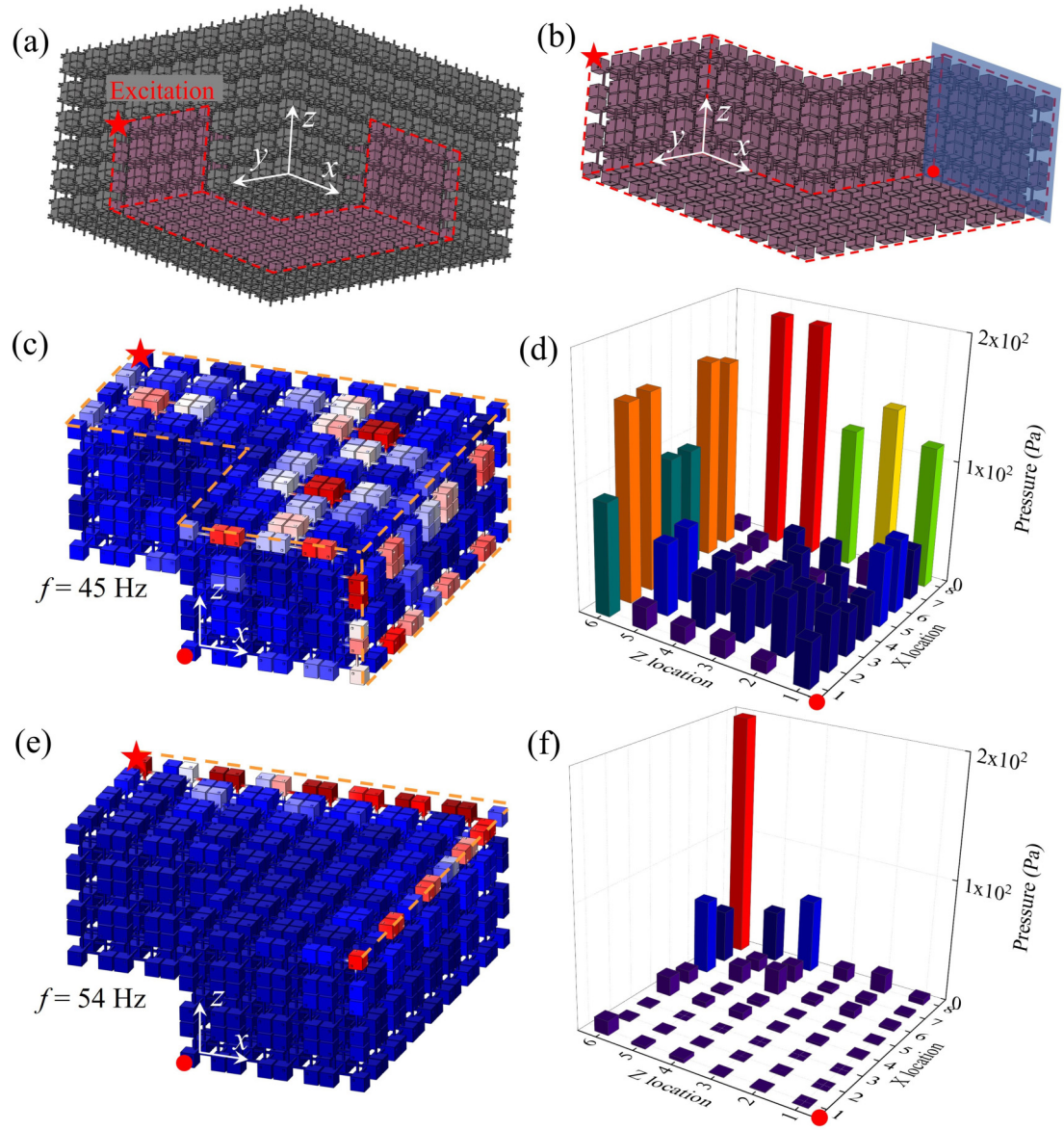

FIG. 12. Waveguiding in the twisted 2D path. (a) Schematic diagram of the proposed structure for 2D twisted waveguiding. (b) Local plot of the extracted R_{VIII} part where the output face is marked by blue shading. (c) Wave propagation mode of $f = 45$ Hz where surface-restricted wave propagation can be observed. (d) Pressure map at the output face of $f = 45$ Hz. (e) Wave propagation mode of $f = 54$ Hz where edge-restricted wave propagation can be observed. (f) Pressure map at the output face of $f = 54$ Hz.

shown in Fig. 11(b), where the yellow star indicates excitation, and the red, blue, and green dots are, respectively, corner, hinge, and surface detectors. Note that there are 6 corner detectors, 9 hinge detectors, and 27 surface detectors, hence the corresponding mean pressure values are calculated for reference. By observing the result in Fig. 11(c), we notice the whole frequency range can be divided into several different parts based on the dominant states. For example, the mean pressure obtained of the surface detector in the green region (44.9–47.4 Hz) is obviously higher than the hinge and corner detectors. The propagation mode of the surface state at 47.2 Hz (green star) is shown in Fig. 11(d), in which the wave can only propagate along the surfaces. We also notice that the hinge regions (blue regions) are not continuous, which matches the conclusion in Fig. 10(b). The propagation mode in Fig. 11(e) demonstrates the existence of edge-restricted wave propagation at the frequency range of hinge states. Comparatively, the corner detectors only receive one pressure peak at 60.3 Hz (red star), of which the pressure is highly confined at the corners [as depicted in Fig. 11(f)]. For the gray regions, all detectors receive near-zero sound pressure, which is a hallmark of the bandgap state. The prediction is confirmed by the pressure distribution of 66 Hz in Fig. 11(g), where the sound energy is obviously confined around the excitation region.

VII. WAVEGUIDING IN TWISTED PATH

A. Twisted 2D path

Waveguiding, a design to ensure a wave can only propagate along a designed path, is one of the most important applications of topological metamaterials. In Secs. V and VI, the

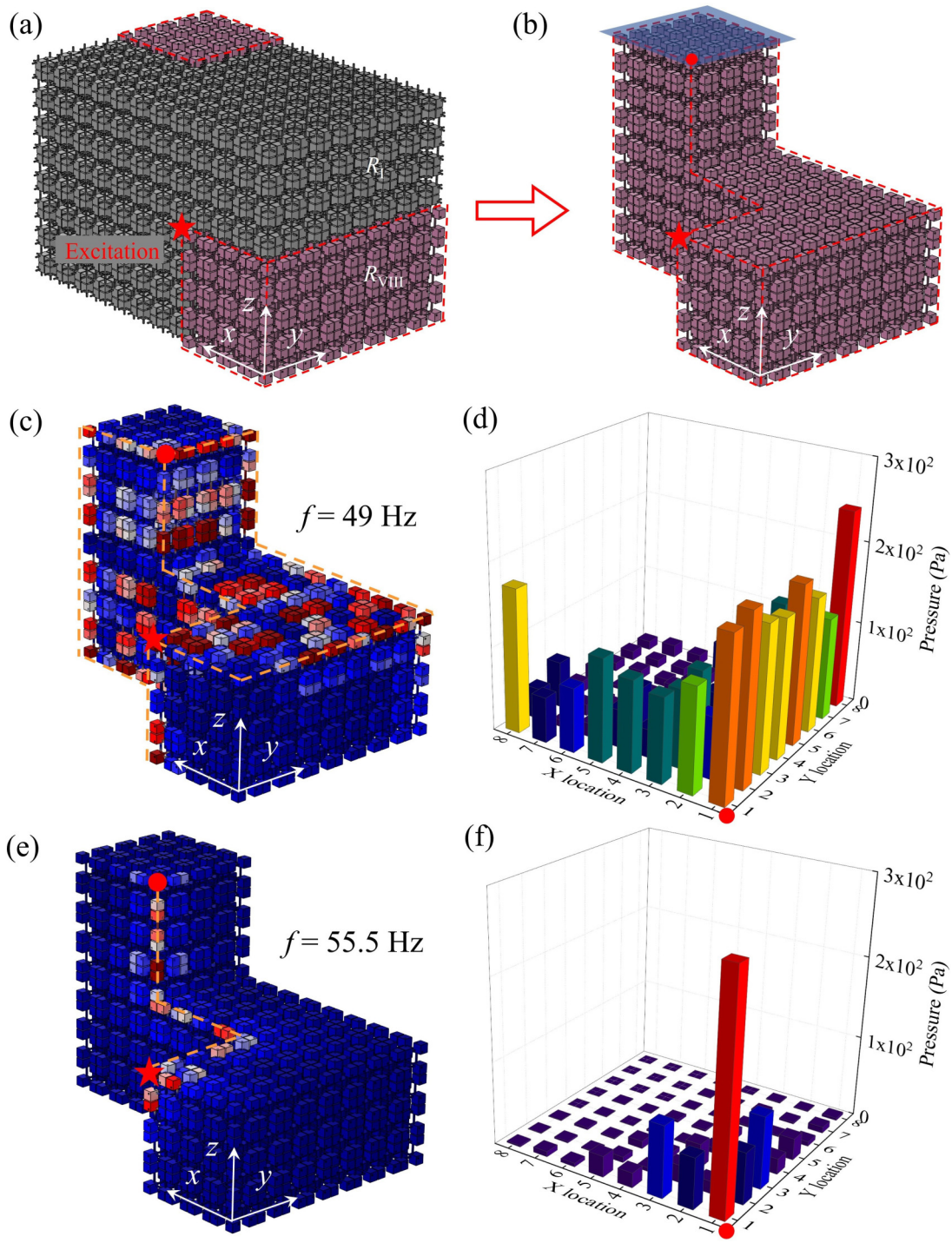

FIG. 13. Waveguiding in the twisted 3D path. (a) Schematic diagram of the proposed structure for 3D twisted waveguiding. (b) Local plot of the extracted R_{VIII} part where the output face is marked by blue shading. (c) Wave propagation mode of $f = 49$ Hz where surface-restricted wave propagation can be observed. (d) Pressure map at the output face of $f = 49$ Hz. (e) Wave propagation mode of $f = 55.5$ Hz where edge-restricted wave propagation can be observed. (f) Pressure map at the output face of $f = 55.5$ Hz.

surface- and edge-restricted waveguiding along a straight path has been demonstrated. However, waveguiding in a twisted path has not been studied yet. The demonstration of twisted waveguiding can not only extend the application scenario but also validate the robustness of waveguiding against sharp corners. Given this, we propose a structure in Fig. 12(a), which is composed of an "L"-shape nontrivial region (purple region) and the surrounding trivial region (gray region). These two regions are respectively made up of R_{VIII} and R_{I} unit cells. Therefore, two bent hinge paths and three bent surface paths are formed. As graphically illustrated in Fig. 12(b), we first give a sound source at the top left corner (red star) of the input surface and detect the pressure map of the output surface (blue shadow). When the excitation frequency ($f = 45$ Hz) is in

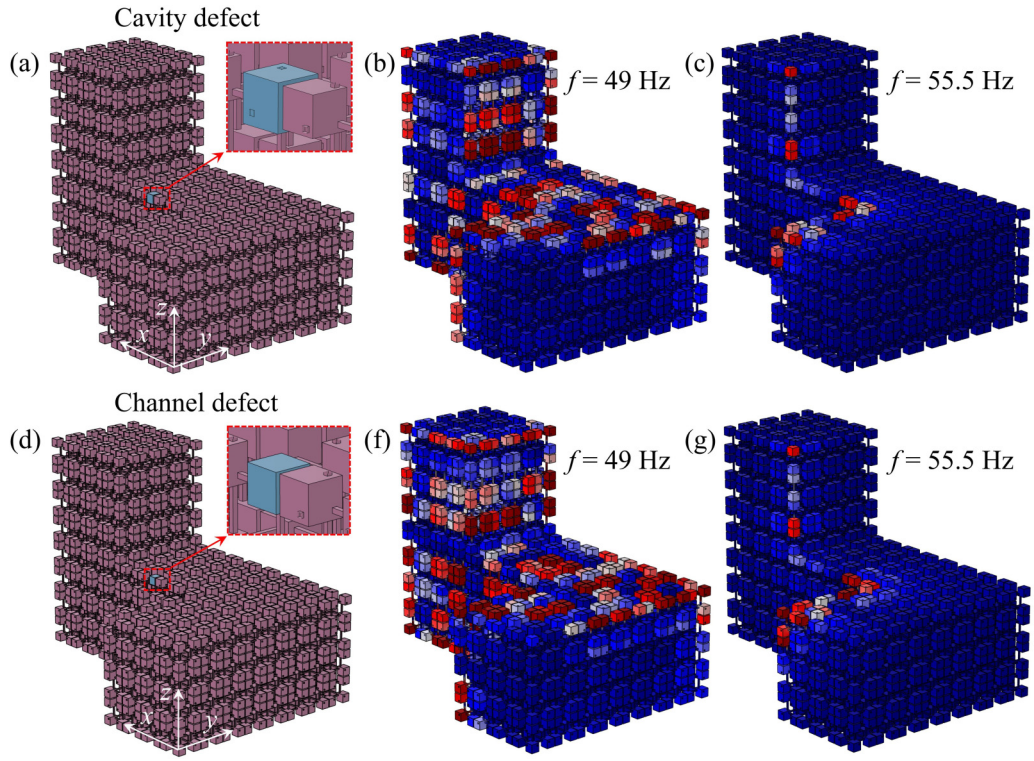

FIG. 14. Robustness of waveguiding. (a) Schematic diagram of the proposed structure with cavity defect. (b) Surface waveguiding with cavity defect at 49 Hz. (c) Edge waveguiding with cavity defect at 55.5 Hz. (a) Schematic diagram of the proposed structure with channel defect. (b) Surface waveguiding with channel defect at 49 Hz. (c) Edge waveguiding with channel defect at 55.5 Hz.

the surface states region, i.e., the green region in Fig. 11(c), we can notice from Fig. 12(c) the sound wave will propagate along the intersurfaces neighboring the source. The pressure map of the output surface in Fig. 12(d) also demonstrates the phenomenon quantitatively. Note that the coordinate origin of the pressure map is located at the highlighted red cycle in the output surface. Subsequently, we adjust the excitation frequency to 54 Hz, which belongs to the hinge states region, i.e., the blue region in Fig. 11(c). It can be noticed from Fig. 12(e) that the sound wave transports along the interedge strictly without significant energy loss at the 90 ° corner. The pressure map in Fig. 12(f) provides quantitative evidence, in which the detected pressure at the top right corner (exit of hinge) is much higher than other locations.

B. Twisted 3D path

The majority of the previous research [11,55] only showed waveguiding in the 2D path as presented in Secs. VI and VII A. However, the twisted 3D waveguiding that is essential for signal detection and processing is still unexplored. Due to this research gap, we further propose a structure in Fig. 13(a), which consists of one interedge and two intersurfaces between the R_{VIII} and R_{I} parts. It can be noticed the waveguiding path has two 90 ° corners in the xy and xz planes, respectively, so that a 3D path for surface- and edge-restricted waveguiding is designed. In Fig. 13(b), it shows a local plot of R_{VIII} parts, where the red star and red cycle represent the excitation source and the coordinate origin of pressure maps, respectively. Moreover, the output face is marked by a blue shadow. After giving a 49 Hz excitation that belongs to the surface states region, we can observe obvious surface-restricted wave propagation along the two intersurfaces in this twisted 3D structure from Fig. 13(c). To provide a quantitative comparison, the pressure distribution of the output face is shown in Fig. 13(d), where the pressure of two edges neighboring the coordinate origin is obviously higher than the other locations. When the excitation frequency turns to the hinge states region such as 55.5 Hz, the edge-restricted wave propagation along the 3D path without significant energy loss is obtained in Fig. 13(e). The pressure map in Fig. 13(f) also demonstrates that the sound wave only propagates along the designed edge while it is insulated for the bulk and surface.

C. Robustness of waveguiding

One of the most peculiar properties of topological states is the robustness against sharp corners and minor imperfections. After demonstrating waveguiding along paths with 90 ° corners in Secs. VII A and VII B, we further investigate two types of structure defects, i.e., cavity defect and channel defect for their robustness against minor imperfections. As shown in Fig. 14(a), the cavity defect, in which the blue cavity has a larger side length ($L = 0.34$ m) than normal cavities ($L = 0.3$ m), indicates fabrication imperfection. The surface-restricted and edge-restricted waveguiding with cavity defect can be clearly observed in Figs. 14(b) and 14(c). For surface waveguiding, sound pressure propagates along the two interfaces strictly without obvious distinction when compared to a normal case. In terms of edge waveguiding, the wave

transmission at the defect location seems to be influenced, but from a global viewpoint, we can still notice robust waveguiding along the designed path. In addition, the channel defect in Fig. 14(d), representing possible air channel blocking after prolonged service, is introduced at the blue cavity by deleting several air channels. Despite the defect, both surface and edge waveguiding can still be clearly observed in Figs. 14(f) and 14(g), respectively. Therefore, we successfully demonstrate the robustness of the designed waveguiding structure against minor imperfections in this section.

VIII. CONCLUSION

In conclusion, we establish 3D TIs that are composed of eight air cavities and corresponding inter- or intracell air channels. An equivalent electric system is introduced to provide a theoretical approach with analysis for the dispersion relation. Very good agreement between the numerical solutions and the analytical result is obtained. Thanks to the three tuning degrees of freedom, i.e., l_x, l_y, and l_z, the model can obtain both complete and directional bandgaps. Moreover, we showed the symmetry properties of eigenmodes at higher symmetry points that are closely related to air cavity distance. To quantitatively characterize the topological phases, we introduced the concept of fractional bulk polarization with a map plot. From the bulk polarization map, it is concluded that the topological phases at different higher symmetry points, i.e., X, Y, and Z are independently related to the air cavity distance along the corresponding directions, i.e., l_x, l_y, and l_z.

Subsequently, three different 1D FOTIs are established to prove that TPIM occurs only if the unit cells spread along the direction with phase conflict. The surface-restricted wave propagation along different planes is obtained by applying this property. For a higher-order model, e.g., SOTI, wave propagation becomes edge restricted rather than the surface. As for TOTI, the dimensional hierarchy is followed such that the sound wave is concentrated at the corners. Therefore, it is concluded that wave propagation can be confined in a lower dimension, i.e., surface-edge-corner with a higher-order TI, i.e., FOTI-SOTI-TOTI. Finally, the surface-restricted and edge-restricted waveguides in both the 2D twisted path and the 3D twisted path are demonstrated. We believe the proposed 3D TI has great application potential in acoustic sensing, 3D acoustic manipulation, acoustic field concentration, etc.

The data that support the findings of this study are available from the corresponding author upon reasonable request.

ACKNOWLEDGMENT

The work described in this paper was supported by City University of Hong Kong (Project No. ARG 9667253).

The authors declare that they have no known competing financial interests or personal relationships that could have appeared to influence the work reported in this paper.

[1] F. D. M. Haldane, Model for a quantum Hall effect without Landau levels: Condensed-matter realization of the "parity anomaly," Phys. Rev. Lett. **61**, 2015 (1988).

[2] M. Z. Hasan and C. L. Kane, *Colloquium*: Topological insulators, Rev. Mod. Phys. **82**, 3045 (2010).

[3] A. Ni and Z. Shi, Robust elastic wave transport in zone-folding induced topological hierarchical metamaterials, Int. J. Mech. Sci. **251**, 108336 (2023).

[4] G. Wang, T. Wang, Z. Chen, Z. Zhu, and C. W. Lim, A novel 3D topological metamaterial for controllability of polarization-dependent multilayer elastic waves, Composites, Part B **275**, 111341 (2024).

[5] Y. Yang, Y. F. Xu, T. Xu, H.-X. Wang, J.-H. Jiang, X. Hu, and Z. H. Hang, Visualization of a unidirectional electromagnetic waveguide using topological photonic crystals made of dielectric materials, Phys. Rev. Lett. **120**, 217401 (2018).

[6] L. Lu, J. D. Joannopoulos, and M. Soljačić, Topological photonics, Nat. Photon. **8**, 821 (2014).

[7] M. Yan, J. Lu, F. Li, W. Deng, X. Huang, J. Ma, and Z. Liu, On-chip valley topological materials for elastic wave manipulation, Nat. Mater. **17**, 993 (2018).

[8] S. Li, D. Zhao, H. Niu, X. Zhu, and J. Zang, Observation of elastic topological states in soft materials, Nat. Commun. **9**, 1370 (2018).

[9] A. Ni and Z. Shi, Subwavelength tunable topological interface modes in metamaterial beams on elastic foundation, Phys. Lett. A. **466**, 128734 (2023).

[10] C. He, X. Ni, H. Ge, X.-C. Sun, Y.-B. Chen, M.-H. Lu, X.-P. Liu, and Y.-F. Chen, Acoustic topological insulator and robust one-way sound transport, Nat. Phys. **12**, 1124 (2016).

[11] G. Wang, Y. Wei, Z. Chen, and C. W. Lim, Controllable subwavelength topological rainbow trapping in water-filling acoustic metamaterials, Appl. Acoust. **207**, 109366 (2023).

[12] Z. Chen, G. Wang, and C. W. Lim, Periodically alternated elastic support induced topological phase transition in phononic crystal beam systems, Int. J. Solids Struct. **239**, 111461 (2022).

[13] Z. Chen, G. Wang, F. Shi, and C. W. Lim, Analytical modeling and numerical analysis for tunable topological phase transition of flexural waves in active sandwiched phononic beam systems, Int. J. Mech. Sci. **223**, 107292 (2022).

[14] A. Ni and Z. Shi, Topological metamaterial plates: Numerical investigation, experimental validation and applications, Eng. Struct. **275**, 115288 (2023).

[15] S.-Y. Huo, J.-J. Chen, H.-B. Huang, Y.-J. Wei, Z.-H. Tan, L.-Y. Feng, and X.-P. Xie, Experimental demonstration of valley-protected backscattering suppression and interlayer topological transport for elastic wave in three-dimensional phononic crystals, Mech. Syst. Signal Proc. **154**, 107543 (2021).

[16] S. Shan, Z. Liu, L. Cheng, and Y. Pan, Metamaterial-enhanced coda wave interferometry with customized artificial frequency-space boundaries for the detection of weak structural damage, Mech. Syst. Signal Proc. **174**, 109131 (2022).

[17] L. Y. L. Ang, Y. K. Koh, and H. P. Lee, Acoustic metamaterials: A potential for cabin noise control in automobiles and armored vehicles, Int. J. Appl. Mech. **8**, 1650072 (2016).

[18] G. Wang, F. Shi, Z. Chen, Y. Yu, and C. W. Lim, Controllable flexural wave bandgap in extensible metamaterial beams with

embedded multiple resonators, Continuum Mech. Thermodyn. (2023).
[19] S. Qi, M. Oudich, Y. Li, and B. Assouar, Acoustic energy harvesting based on a planar acoustic metamaterial, Appl. Phys. Lett. **108**, 263501 (2016).
[20] Z. Wen, Y. Jin, P. Gao, X. Zhuang, T. Rabczuk, and B. Djafari-Rouhani, Topological cavities in phononic plates for robust energy harvesting, Mech. Syst. Signal Proc. **162**, 108047 (2022).
[21] Z. Xiong, Z.-K. Lin, H.-X. Wang, X. Zhang, M.-H. Lu, Y.-F. Chen, and J.-H. Jiang, Corner states and topological transitions in two-dimensional higher-order topological sonic crystals with inversion symmetry, Phys. Rev. B **102**, 125144 (2020).
[22] F. Schindler, A. M. Cook, M. G. Vergniory, Z. Wang, S. S. Parkin, B. A. Bernevig, and T. Neupert, Higher-order topological insulators, Sci. Adv. **4**, eaat0346 (2018).
[23] F. Meng, Y. Chen, W. Li, B. Jia, and X. Huang, Realization of multidimensional sound propagation in 3D acoustic higher-order topological insulator, Appl. Phys. Lett. **117**, 151903 (2020).
[24] B. Xie, H.-X. Wang, X. Zhang, P. Zhan, J.-H. Jiang, M. Lu, and Y. Chen, Higher-order band topology, Nat. Rev. Phys. **3**, 520 (2021).
[25] G. Wang, Z. Chen, and C. W. Lim, Subwavelength path-switchable wave routing and topological corner states for a higher-order topological insulator, J. Sound Vibr. **564**, 117869 (2023).
[26] M. Serra-Garcia, V. Peri, R. Süsstrunk, O. R. Bilal, T. Larsen, L. G. Villanueva, and S. D. Huber, Observation of a phononic quadrupole topological insulator, Nature (London) **555**, 342 (2018).
[27] X. Ni, M. Li, M. Weiner, A. Alù, and A. B. Khanikaev, Demonstration of a quantized acoustic octupole topological insulator, Nat. Commun. **11**, 2108 (2020).
[28] Z. Zhang, B. Hu, F. Liu, Y. Cheng, X. Liu, and J. Christensen, Pseudospin induced topological corner state at intersecting sonic lattices, Phys. Rev. B **101**, 220102(R) (2020).
[29] Z. Wang, Q. Wei, H.-Y. Xu, and D.-J. Wu, A higher-order topological insulator with wide bandgaps in Lamb-wave systems, J. Appl. Phys. **127**, 075105 (2020).
[30] H. Xue, Y. Yang, F. Gao, Y. Chong, and B. Zhang, Acoustic higher-order topological insulator on a kagome lattice, Nat. Mater. **18**, 108 (2019).
[31] Z. Zhang, H. Long, C. Liu, C. Shao, Y. Cheng, X. Liu, and J. Christensen, Deep-subwavelength holey acoustic second-order topological insulators, Adv. Mater. **31**, 1904682 (2019).
[32] X.-L. Sheng, C. Chen, H. Liu, Z. Chen, Z.-M. Yu, Y. X. Zhao, and S. A. Yang, Two-dimensional second-order topological insulator in graphdiyne, Phys. Rev. Lett. **123**, 256402 (2019).
[33] B.-Y. Xie, G.-X. Su, H.-F. Wang, H. Su, X.-P. Shen, P. Zhan, M.-H. Lu, Z.-L. Wang, and Y.-F. Chen, Visualization of higher-order topological insulating phases in two-dimensional dielectric photonic crystals, Phys. Rev. Lett. **122**, 233903 (2019).
[34] C.-B. Hua, R. Chen, B. Zhou, and D.-H. Xu, Higher-order topological insulator in a dodecagonal quasicrystal, Phys. Rev. B. **102**, 241102(R) (2020).
[35] H. Xue, Y. Yang, G. Liu, F. Gao, Y. Chong, and B. Zhang, Realization of an acoustic third-order topological insulator, Phys. Rev. Lett. **122**, 244301 (2019).
[36] M. Xiao, G. Ma, Z. Yang, P. Sheng, Z. Zhang, and C. T. Chan, Geometric phase and band inversion in periodic acoustic systems, Nat. Phys. **11**, 240 (2015).
[37] W.-P. Su, J. R. Schrieffer, and A. J. Heeger, Solitons in polyacetylene, Phys. Rev. Lett. **42**, 1698 (1979).
[38] C. H. Lee, S. Imhof, C. Berger, F. Bayer, J. Brehm, L. W. Molenkamp, T. Kiessling, and R. Thomale, Topolectrical circuits, Commun. Phys. **1**, 39 (2018).
[39] S. Liu, W. Gao, Q. Zhang, S. Ma, L. Zhang, C. Liu, Y. J. Xiang, T. J. Cui, and S. Zhang, Topologically protected edge state in two-dimensional Su–Schrieffer–Heeger circuit, Research **2019**, 8609875 (2019).
[40] G. W. Stewart, Acoustic wave filters, Phys. Rev. **20**, 528 (1922).
[41] S. Zhang, C. Xia, and N. Fang, Broadband acoustic cloak for ultrasound waves, Phys. Rev. Lett. **106**, 024301 (2011).
[42] Z. Chen, Y. B. Chong, K. M. Lim, and H. P. Lee, Reconfigurable 3D printed acoustic metamaterial chamber for sound insulation, Int. J. Mech. Sci. **266**, 108978 (2024).
[43] D. Liao, Z. Zhang, Y. Cheng, and X. Liu, Engineering negative coupling and corner modes in a three-dimensional acoustic topological network, Phys. Rev. B **105**, 184108 (2022).
[44] Z. Zhang, Y. Cheng, and X. Liu, Subwavelength higher-order topological insulator based on stereo acoustic networks, J. Appl. Phys. **129**, 135101 (2021).
[45] W. Zhou, B. Wu, Z. Chen, W. Chen, C. W. Lim, and J. N. Reddy, Actively controllable topological phase transition in homogeneous piezoelectric rod system, J. Mech. Phys. Solids **137**, 103824 (2020).
[46] F. Liu and K. Wakabayashi, Novel topological phase with a zero Berry curvature, Phys. Rev. Lett. **118**, 076803 (2017).
[47] F. Liu, H.-Y. Deng, and K. Wakabayashi, Topological photonic crystals with zero Berry curvature, Phys. Rev. B **97**, 035442 (2018).
[48] Y. Chen, Z. Lan, and J. Zhu, Second-order topological phases in C_{4v}-symmetric photonic crystals beyond the two-dimensional Su-Schrieffer–Heeger model, Nanophotonics **11**, 1345 (2022).
[49] F. Liu, H.-Y. Deng, and K. Wakabayashi, Helical topological edge states in a quadrupole phase, Phys. Rev. Lett. **122**, 086804 (2019).
[50] Z. Wang, H. Li, Z. Wang, Z. Liu, J. Luo, J. Huang, X. Wang, R. Wang, and H. Yang, Straight-angled corner state in acoustic second-order topological insulator, Phys. Rev. B **104**, L161401 (2021).
[51] S. Nanthakumar, X. Zhuang, H. S. Park, C. Nguyen, Y. Chen, and T. Rabczuk, Inverse design of quantum spin Hall-based phononic topological insulators, J. Mech. Phys. Solids **125**, 550 (2019).
[52] V. G. M. Annamdas and C. K. Soh, Application of metamaterial surface plasmon and waveguide for robotic-arm based structural health monitoring, J. Nondestruct. Eval. **37**, 1 (2018).
[53] S. Shan, F. Wen, and L. Cheng, Purified nonlinear guided waves through a metamaterial filter for inspection of material microstructural changes, Smart Mater. Struct. **30**, 095017 (2021).
[54] Y. Ota, F. Liu, R. Katsumi, K. Watanabe, K. Wakabayashi, Y. Arakawa, and S. Iwamoto, Photonic crystal nanocavity based on a topological corner state, Optica **6**, 786 (2019).
[55] Y. Dong, Y. Wang, C. Ding, S. Zhai, and X. Zhao, Tunable topological valley transport in acoustic topological metamaterials, Phys. B (Amsterdam, Neth.) **605**, 412733 (2021).